

## ARTICLE

# Recent Developments of Hydrogel Based Solar Water Purification Technology

Received 00th January 20xx,  
Accepted 00th January 20xx

DOI: 10.1039/x0xx00000x

Shudi Mao,<sup>a</sup> Md Abu Hasan Johir,<sup>a</sup> Casey Onggowarsito,<sup>a</sup> An Feng,<sup>a</sup> Long D. Nghiem<sup>a</sup> and Qiang Fu<sup>a\*</sup>

Water scarcity is a severe problem all over the world, however most current large-scale water purification technologies are energy-intensive and require high capital and maintenance costs. Recently, hydrogel-based solar water purification technologies have attracted increasing attention due to their advantages, including easy preparation, less energy intensive, high efficient solar absorption and utilization. This review summarized recent advances in the development of novel hydrogel materials from two perspectives: improving solar-thermal conversion efficiency, and facilitating water transport. The main strategies to achieve higher conversion efficiency include choosing good solar absorbers, constructing a surface to reduce light reflection and reducing heat loss. Adjusting wettability, tuning the physio-chemical properties of internal channels, and increasing the intermediate water content to lower the water vaporization enthalpy are the three main approaches of rapid water transport. This review also provides new insights on future directions and remaining challenges in this field.

## 1. Introduction

As an essential substance of life, water is one of the most essential resources for ecological well-beings and economic development. Rapid population growth, economic progress, agriculture industrialisation, dietary changes, and climate change<sup>1,2</sup> have led to nearly eightfold increase in fresh water demand between the 1990s and the 2010s.<sup>3</sup> Despite recent and worldwide economic progress, by 2025, one-third of the world population will still face water scarcity. The Massachusetts Institute of Technology MIT Integrated Global System Model Water Resource System predicted that by 2050, about 52% of the world's projected population (9.7 billion) would live in water-stressed regions.<sup>4</sup> Therefore, there is an ever increasing need to develop efficient, affordable and scalable purification technologies to obtain fresh water from abundant sources such as seawater, brackish water and wastewater that are independent from the hydrological cycle.

Freshwater can be extracted from the ocean or brackish water sources by thermal distillation or filtration technologies.<sup>5-9</sup> Thermal distillation processes such as multi-stage flash distillation,<sup>10</sup> multiple effect distillation,<sup>11</sup> and membrane distillation have been widely used for seawater desalination applications, specially in the Middle East. These technologies require significant thermal energy input, thus, many of them are co-located with and utilize waste heat from thermal power plants to lower energy consumption. Even when co-locating with thermal power plants, the energy consumption of these conventional thermal distillation technologies is still quite high,

in the range of 5-60 kWh/m<sup>3</sup> of produced freshwater.<sup>7,12</sup> Filtration-based water purification technologies, such as reverse osmosis (RO)<sup>13</sup> and electrodialysis,<sup>14</sup> rely mainly on the separation salt from water via a semipermeable membrane. RO has been commercialized at large scale and can achieve relatively low energy consumption of *ca.* 3-4 kWh/m<sup>3</sup> of produced freshwater from seawater.<sup>15-17</sup> However, the RO membrane is susceptible to fouling during operation, and hence frequent chemical cleaning is required.<sup>18</sup> In the electrodialysis process, cation and anion exchange membranes are used to selectively transport salts away from the saline feedwater solution. Electrodialysis is only suitable for brackish water that is about a fifth of the salinity of seawater<sup>19</sup> and the energy consumption is also quite energy.<sup>20</sup> Hence, most of the current full-scale water purification technologies consume a significant amount of energy and are therefore costly, encouraging the researchers to develop next-generation cost-effective water purification technologies. These cost-effective water purification technologies will reduce energy consumption or will use renewable energy.

As the most abundant and renewable energy source, solar energy can be used for freshwater production.<sup>21</sup> Solar still is the simple solar water purification technology.<sup>22</sup> Figure 1a illustrates a conventional solar still system, consisting of a sloping glass cover, a black basin with seawater or wastewater, and a thermally insulated enclosure. Because the black basin absorbs solar energy, water evaporates and then condenses on the inner surface of the shelter. As a result, freshwater can be obtained at the cover's lower end. Unfortunately, the solar vapor generation (SVG) efficiency of such solar still system is too low (*ca.* 1-5 L m<sup>-2</sup> d<sup>-1</sup>)<sup>23</sup> to be widely utilized due to insufficient solar absorption and significant thermal loss. To overcome this

<sup>a</sup>Centre for Technology in Water and Wastewater, School of Civil and Environmental Engineering, University of Technology Sydney, NSW 2007, Australia

\*Corresponding author. E-mail address: Qiang.Fu@uts.edu.au

Electronic Supplementary Information (ESI) available. See DOI: 10.1039/x0xx00000x

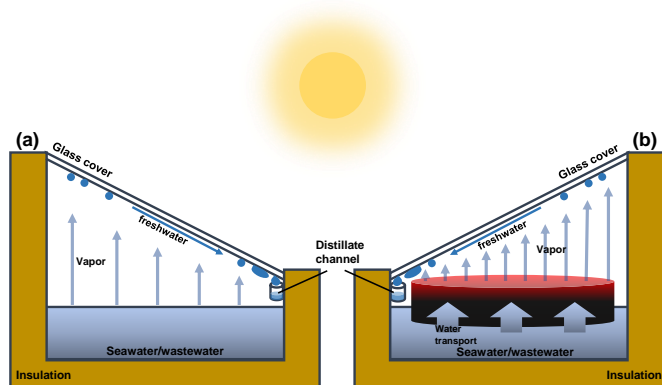


Figure 1. Schematic illustrations of a single slope (a) solar still and (b) hydrogel based material platform for solar water purification.

challenge, novel hydrogel materials have been introduced and incorporated into traditional solar still (Figure 1b). The thin red layer in Figure 1b is above the water surface. It can localize heat in the evaporation interface, reduce heat loss to bulk water, and improve the solar-thermal conversion efficiency, vapor generation rate, and freshwater productivity.<sup>24–28</sup> These materials commonly composed of solar absorbers which can transfer solar energy into thermal energy, and porous, low-conductivity, hydrophilic materials that can reduce heat loss and transport water to the evaporation interface. Accordingly, considerable effort has been focused on improving solar-thermal conversion efficiency, enhancing heat insulation, and speeding up water transport. In 2018, Zhao *et al.*<sup>25</sup> introduced a hydrogel-based material to reduce the energy demand for evaporation and improve solar vapor generation efficiency. Specific water states in polymer hydrogels caused by the distinct preference for water molecules of the hydrophilic polymer chains can make the water more active, thereby facilitating the evaporation process. Since then, as a landmark study, it has heightened interest in this field, and more and more publications on hydrogel-based solar water purification have appeared recently.

Although the development of hydrogel-materials for solar water purification is still in its early stages, there have been many research papers published in this field. A timely, thorough review of the recent achievements will highlight key research findings and reveal significant research trends in this field. This review summarises the design principles of hydrogel based materials for solar water purification from two primary directions: improving solar-thermal conversion efficiency, and facilitating water transport with examples from the recent three years' representative research. We also put forward prospects on the future directions and remaining challenges in this field.

## 2. Solar-thermal conversion enhancement

Solar-thermal conversion is the core step of Solar Water Purification, consisting of light-harvesting, photothermal conversion and heat insulation. The light-harvesting competence of the materials platform, especially the solar

absorbers, is the precondition for attaining sufficient photothermal conversion. Reflection, transmission and absorption might happen to the solar radiation when it strikes the solar absorbers' surface, but only the absorbed irradiation is the net energy input for subsequent conversion. Thus, solar absorbers with high irradiation absorptivity and topographical and geometrical designs that reduce reflection and transmission are vital for achieving high conversion efficiency.<sup>29</sup> The absorbed sunlight energy can be converted into thermal energy by the solar absorbers instead of being re-emitted. A large number of nanomaterials have been employed as solar absorbers, and various photothermal conversion mechanisms are presented based on the different interactions between electromagnetic radiation and the specific categories of solar absorbers.<sup>30, 31</sup> In the end, the generated heat will be confined in the evaporation interface layer through the heat insulation designs<sup>27, 32, 33</sup> to reduce heat loss to bulk water and thereby improve the efficiency of heat utilization.

Since a diverse array of factors noted above collaboratively contribute to the solar-thermal conversion competence of the entire solar water purification system, the metric energy conversion efficiency ( $\eta$ ) has been proposed to quantitatively assess its solar-thermal conversion performance, which can be calculated according to equation 1:<sup>34</sup>

$$\eta = \frac{\dot{m} \times h_v}{C_{opt} \times P_0} \quad (1)$$

where  $\dot{m}$ ,  $h_v$ ,  $C_{opt}$  and  $P_0$  refer to the steady-state evaporation mass flux, the equivalent vaporization latent enthalpy of the water in the hydrogel, the optical concentration on the absorbers' surface, and the solar irradiation power (normally 1 sun or 1 kW m<sup>-2</sup>), respectively.

In order to enhance energy conversion efficiency, considerable efforts have been devoted to choosing appropriate solar absorbers, modifying surface topography to reduce light reflection, and mitigating heat loss accordingly.

### 2.1 Solar absorbers

Choosing an appropriate solar absorber with full-spectrum strong solar absorption and high solar-thermal conversion capacity is one of the vital design principles. Plentiful nanomaterials have been adapted as solar absorbers in solar water purification, including inorganic semiconductors, plasmonic nanoparticles, carbon-based materials, and conjugated polymers. Different solar absorbers exhibit diverse solar-thermal conversion mechanisms and thus have different selection principles.

**2.1.1 Inorganic Semiconductors** Semiconductors have been extensively used as solar absorbers due to their highly tunable energy band and inherent thermalization effect.<sup>35–37</sup> Under light illumination, when the exciting energy is higher than the semiconductors band-gap, electron-hole pairs are generated. Then, electrons and holes relax to the conduction and valence bands' edges, and the energy is released in the form of phonons or photons.<sup>38</sup> The non-radiative relaxed phonons can incur lattice localized heating to finally realize the transformation from light to heat.<sup>30, 31</sup> In the entire photothermal conversion process, the band-gap width is a critical determinant of the

amount of energy and heat that can be released. For the solar spectrum, the majority of the radiant energy lies in the infrared ( $\sim 52\%$ ), visible ( $\sim 45\%$ ) and ultraviolet ( $\sim 3\%$ ) wavelength, ranging from 300 to 2500 nm.<sup>39</sup> Since the infrared band occupies the largest proportion, the narrow band-gap semiconductor nanomaterials that can absorb more infrared energy are more suitable as solar absorbers.<sup>37</sup>

For instance, as a widely used light-harvesting semiconductor,  $\text{TiO}_2$  has been used as solar absorbers for preparing hydrogel materials.<sup>40–43</sup> However, under 1 sun, these hydrogels showed a low evaporation rate of  $<1.5 \text{ kg m}^{-2} \text{ h}^{-1}$  and a low energy conversion efficiency of  $<80\%$ . This can be attributed to the wide intrinsic band-gap of  $\text{TiO}_2$  of *ca.* 3 eV, which corresponds to the absorption of UV-light (wavelength  $<400 \text{ nm}$ ).<sup>37,44,45</sup> In contrast, the  $\text{Ti}_2\text{O}_3$  with an extremely narrow band-gap of  $\sim 0.09 \text{ eV}$  exhibits excellent energy conversion performance. Guo *et al.*<sup>24</sup> incorporated  $\text{Ti}_2\text{O}_3$  nanoparticles into sponge-like polyvinyl alcohol (PVA) hydrogel with interconnected pores (Figure 2a). The SEM and the EDS mapping images (Figure 2b–d) also suggested the  $\text{Ti}_2\text{O}_3$  nanoparticles were uniformly distributed in the network. The optimized samples (LASG3, LASG4 and LASG5, Figure 2e and 2f) showed a relatively high solar absorption efficiency of  $>96\%$  and a low reflectance over a broadband of the standard solar spectrum. Correspondingly, the resultant  $\text{Ti}_2\text{O}_3/\text{PVA}$  hydrogels showed an extremely high evaporation rate of  $3.6 \text{ kg m}^{-2} \text{ h}^{-1}$  and an excellent energy conversion efficiency of *ca.* 90%. In all, semiconducting solar absorbers with a narrow band-gap that can absorb more infrared energy will bring excellent solar-thermal conversion competence to the solar water purification system.

Except for  $\text{TiO}_2$ ,  $\text{MnO}_2$ ,<sup>46,47</sup>,  $\text{Co}_3\text{O}_4$ ,<sup>48</sup>,  $\text{CuO}$ ,<sup>47,49,50</sup> and other transition metal oxides have been employed as solar absorbers. Furthermore, transition metal sulfides (such as  $\text{MoS}_2$ ,<sup>51–54</sup>  $\text{Mo}_2\text{S}_3$ ,<sup>55</sup> and  $\text{Bi}_2\text{S}_3$ ),<sup>56</sup> nitrides (such as  $\text{g-C}_3\text{N}_4$ ,<sup>57</sup>  $\text{TiN}$ ,<sup>40</sup> and  $\text{MoN}/\text{Mo}_2\text{N}$ ),<sup>58</sup> as well as other novel semiconductors (such as  $\text{MXene}$ <sup>51, 59–64</sup> and  $\text{CZTSe}$ )<sup>65, 66</sup> have also shown up in recent research progress, mostly with reasonable evaporation rates between  $1.4$  and  $4 \text{ kg m}^{-2} \text{ h}^{-1}$  and energy conversion efficiencies of  $>80\%$ . In addition, liquid metals, such as gallium and indium alloy (EGaIn) with  $\text{Ga}_2\text{O}_3$  (broad bandgap) layer on the surface to prevent the absorption of sunlight, can also be applied as solar absorbers, introducing a dipole layer to narrow the bandgap.<sup>67</sup>

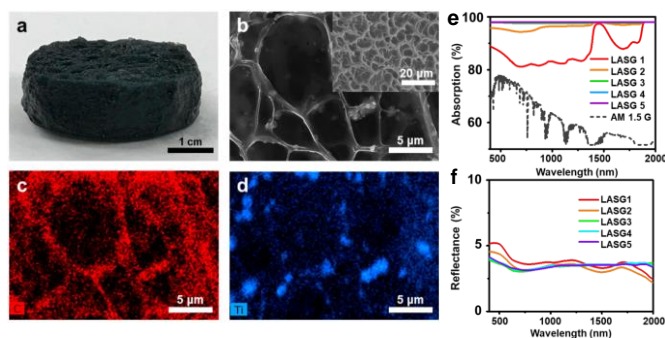
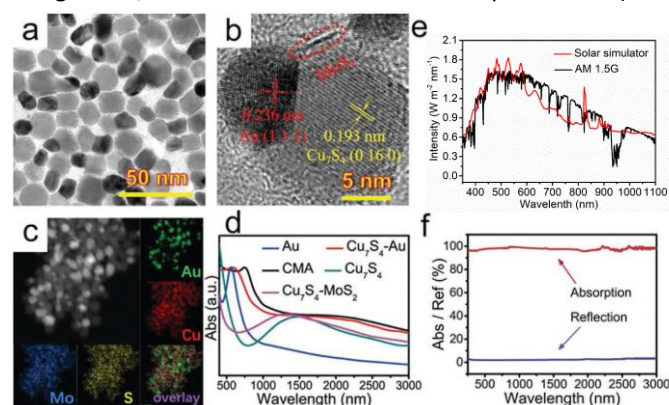


Figure 2. (a) Photo of the as-prepared  $\text{Ti}_2\text{O}_3$ -PVA sponge-like hydrogel sample. (b) SEM image of the sponge-like hydrogel and EDS mapping of (c) carbon and (d) titanium. (e) Absorption and (f) Reflectance spectra in the wavelength range of 200–2000 nm. Reproduced with permission.<sup>24</sup> Copyright 2019, American Chemical Society.

**2.1.2 Plasmonic Nanoparticles** The plasmonic nanomaterials are metallic materials with localized surface plasmon resonance (LSPR) effect, which is the resonant oscillation of free electrons induced by photons when the frequency of photons matches that of the natural metal surface electrons.<sup>31, 68</sup> The LSPR effect causes three consequent phenomena: near-field enhancement, hot electron generation, and photothermal conversion.<sup>31, 69</sup> The Photothermal effect aided by plasmon happens when metal nanoparticles are lit at their resonance wavelengths. Hot electrons are generated as the electrons excited from occupied states to unoccupied ones. By electron-electron scattering, the hot electrons decay, and the hot electron energy can be redistributed, leading to the rapid increasing of nanoparticles surface temperature.<sup>31</sup> Commonly, LSPR spectral band can be expanded by hollow structure, asymmetrical design, particle-size shifts, and dielectric surroundings<sup>70</sup> to compensate for the inherent shortcoming of the narrow absorption spectra of plasmonic nanoparticles caused by their specific geometrics.<sup>37</sup>

Common plasmonic nanoparticles used as solar absorbers include Ag,<sup>71–74</sup> Au,<sup>75</sup> CuS,<sup>76–79</sup> Cu,<sup>42, 80</sup> and so on. Recently, Wang *et al.*<sup>26</sup> reported a novel plasmonic  $\text{Cu}_7\text{S}_4$ - $\text{MoS}_2$ -Au composite nanoparticle (CMA NP) with broad absorption and high photothermal conversion efficiency, which arises from the coupling effect among  $\text{Cu}_7\text{S}_4$ ,  $\text{MoS}_2$  and Au, as well as the comprehensive utilization of their advantages. The  $\text{Cu}_7\text{S}_4$ ,  $\text{MoS}_2$  or Au components can be distinguished by their lattice spacing (Figures 3a and 3b). The EDS mappings (Figure 3c) show the uniform distribution and composition of Au, S, Mo and Cu elements. From the absorption spectra of different NPs shown in Figure 3d, it is found that the visible absorption of Au (LSPR



peak at  $\sim 520 \text{ nm}$ ) and near-infrared absorption of  $\text{Cu}_7\text{S}_4$  (LSPR Figure 3. (a) TEM, (b) HRTEM and (c) HAADF-STEM images as well as corresponding elemental mapping of  $\text{Cu}_7\text{S}_4$ - $\text{MoS}_2$ -Au nanoparticles. (d) Absorption spectra of different nanoparticles including Au,  $\text{Cu}_7\text{S}_4$ ,  $\text{Cu}_7\text{S}_4$ -Au,  $\text{Cu}_7\text{S}_4$ - $\text{MoS}_2$  and CMA NPs. (e) The spectral irradiance density of solar simulator used in test and air mass 1.5 global (AM 1.5 G) tilt solar spectrum. (f) UV-Vis-NIR

absorption and reflection spectra of CMA/PDMS hydrogel measured with an integrated sphere. Reproduced with permission.<sup>26</sup> Copyright 2020, John Wiley and Sons.

peak at  $\sim 1500$  nm) were successfully integrated with the LSPR absorption of CMA NPs. Compared with  $\text{Cu}_7\text{S}_4$ -Au,  $\text{MoS}_2$  can further increase the absorption of CMA NPs. Due to the coupling effect between the  $\text{Cu}_7\text{S}_4$  and Au regions, the absorption around 800 nm was significantly increased. What's more, the intense plasmon-exciton coupling between Au and  $\text{MoS}_2$  was accounted for the redshift in their absorption spectrum. Based on the above findings, it can be concluded that the synergy between these three nanoparticles successfully expands the absorption spectrum and enhances the absorption in the infrared region, which matches well with the solar irradiation spectrum (Figure 3e). When the CMA NPs are embalmed into the polydimethylsiloxane (PDMS) matrix, the entire gel material shows enhanced absorption capacity and low reflection (Figure 3f), leading to excellent evaporation rate ( $3.824 \text{ kg m}^{-2} \text{ h}^{-1}$ ) and energy conversion efficiency (96.6%). Therefore, coupling plasmonic nanoparticles with different absorption domains into one solar absorber is an efficient way to overcome the narrow absorption region of single form plasmonic nanoparticles.

**2.1.3 Carbon-based materials** Carbon-based materials have been used as solar absorbers in various studies in recent years, owing to their excellent light absorption over a broad spectrum, ease of preparation, abundant and low cost. Carbon-based materials include activated carbon,<sup>81-84</sup> polymer<sup>74, 85-88</sup> or biomass<sup>80, 89-93</sup> derived carbide, carbon black<sup>94-99</sup> and various amorphous carbon materials and highly graphitized carbon materials, such as graphene,<sup>54, 57, 61, 72, 75, 100-120</sup> carbon nanotubes (CNTs)<sup>27, 121-128</sup> and their derivatives.

As for amorphous carbon, the broad light absorption ability comes from the continuous energy levels emanating from the hybrid bonds.<sup>129</sup> To address the high reflective energy loss and thus improve their light-harvesting efficiency,<sup>37</sup> considerable efforts have been made in tailoring surface topography,<sup>81</sup> constructing internal channels,<sup>82, 84</sup> and introducing a second phase.<sup>27, 32</sup> Among these amorphous carbons, activated carbon and carbon black are low cost, readily available materials, and can be easily mass-produced. Combining with a reasonable light path and design, the evaporation rate of these materials can reach  $3.86 \text{ kg m}^{-2} \text{ h}^{-1}$ , and the energy conversion efficiency is as high as 92%.<sup>82</sup> Using biochar or polymer as the precursor can reduce fabrication costs<sup>89</sup> or make the derived carbide more design-oriented.<sup>33</sup>

Different from amorphous carbon, the photothermal conversion effect of graphene and highly graphitized carbon materials arises from the conjugated  $\pi$  bonds. A large number of conjugated  $\pi$  bonds enable electrons to be excited at almost every wavelength of the solar spectrum, resulting in various  $\pi$ - $\pi^*$  transitions. The excited electrons relax through electron-phonon coupling, so energy is transferred from the excited electrons to the vibration mode of the entire atomic lattice, which causes the macroscopic temperature of the material to rise.<sup>31</sup> It is noted that a solar water purification system containing reduced graphene oxide (rGO) generally exhibits a

relatively high evaporation rate ( $2.33 - 2.72 \text{ kg m}^{-2} \text{ h}^{-1}$ ) and higher energy conversion efficiency ( $> 90\%$ ) compared to the systems based on graphene and graphene oxide (GO).<sup>57, 61, 72, 75, 100-117</sup> This result may be

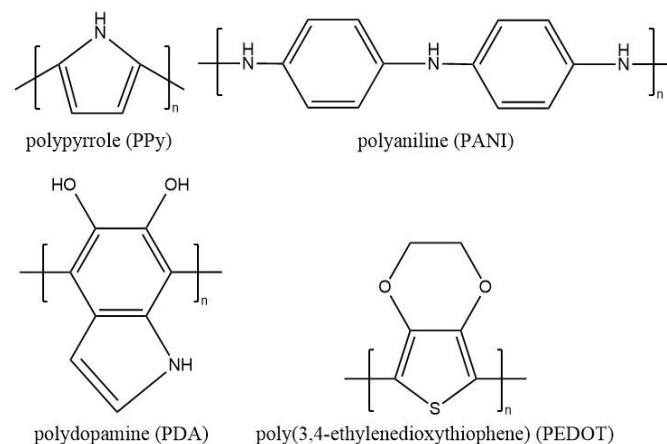


Figure 4. Chemical structures of PPy, PANI, PDA and PEDOT with  $\pi$ -conjugated backbones of  $\text{sp}^2$ -hybridized carbon. attributed to the residual functional groups (*i.e.* epoxy, hydroxyl) on the surface of rGO, which can be further investigated.

As the youngest carbon nanomaterials, carbon dots (CDs)<sup>130-132</sup> have attracted attention due to their broad light absorption spectrum (200-800 nm) and high photothermal conversion efficiency ( $> 90\%$ ), so that CDs can meet the requirements of solar absorbers.<sup>133</sup> To further improve the performance of CDs for solar water purification, future development directions include structure adjustment and surface group modification without lowering crystallinity or wetting properties.

**2.1.4 Conjugated polymers** Apart from the aforementioned inorganic materials, unique, organic polymers with conjugated backbone structures (Figure 4) are often used as a solar absorbers in solar water purification. Due to the  $\pi$ -conjugated backbones of  $\text{sp}^2$ -hybridized carbon, conjugated polymers have splitting energy levels and adjustable band-gaps, resulting in a similar performance to inorganic semiconductors.<sup>37, 134</sup> Similarly, to improve the solar-thermal conversion performance, several strategies have been proposed to reduce the forbidden bandwidth and red-shift the main absorption peak to the NIR region. For conjugated polymers, this is usually accomplished by oxidation doping.<sup>134</sup> In addition, another advantage of polymer solar absorbers is that they have higher compatibility with hydrogel networks, thereby improving manufacturing processability.

A representative polymer solar absorber is polypyrrole (PPy), which has been reported in recent studies.<sup>25, 73, 128, 135-146</sup> For instance, Zhao *et al.*<sup>25</sup> introduced PPy into a PVA-based hydrogel network and achieved a high evaporation rate of  $3.2 \text{ kg m}^{-2} \text{ h}^{-1}$  with an excellent energy conversion efficiency of 94%. In the next year, the same group reported a PPy/chitosan/PVA hydrogel platform that exhibited an enhanced solar vapor generation capacity of  $3.6 \text{ kg m}^{-2} \text{ h}^{-1}$ .<sup>135</sup> Recent research on conjugated polymer solar absorbers has been extended to polyaniline (PANI),<sup>147, 148</sup> poly(3,4-ethylene dioxythiophene) (PEDOT),<sup>149, 150</sup> polydopamine (PDA),<sup>64, 151-154</sup> perovskite hole



layer material DPP-2T,<sup>155</sup> and covalent organic frameworks (COFs).<sup>120, 156</sup> Furthermore, conjugated copolymer materials such as poly(aniline-co-pyrrole)<sup>32</sup> have also shown up in recent research, proving a novel approach for solar water purification by combining the advantages of two polymers.

**2.1.5 Comparison between different solar absorbers** Although many reviews have broadly compared the performance of different solar absorbers, rare research articles can fairly compare their performance under the same experimental conditions. Sun et al.<sup>151</sup> prepared four hydrogels composed of the same polymer materials but different solar absorbers, such as plasmonic nanoparticle CuS, carbon-based material GO, and conjugated polymers PPy and PDA, and conducted solar water evaporation experiments. The calculated evaporation rates are 1.6, 1.66, 1.74 and 1.84 kg m<sup>-2</sup> h<sup>-1</sup> for CuS, GO, PPy and PDA, and their energy conversion efficiencies are 79.6%, 83%, 87% and 92%, respectively. In this study, conjugate polymers showed the best performance compared with plasmonic nanoparticles and carbon-based materials, but this inference is limited to the performance of particular materials under specific conditions. In addition, inorganic semiconductors are not involved in this comparison. It is expected that there will be more research on the application of various solar absorbers and performance comparison, which will provide an insightful perspective on the selection of suitable solar absorbers.

## 2.2 Surface topography modification

The most effective strategy to enhance the light-harvesting capacity of the hydrogel platforms is to tailor surface topography to reduce light reflection.<sup>67, 76, 81, 147, 157, 158</sup> Some materials<sup>76, 147</sup> are porous, so rough surfaces contribute to higher light-harvesting ability. Recently, researchers have proposed novel design methods to tailor undulating surfaces, including mold embossing,<sup>158</sup> *in-situ* template-assisted fabrication,<sup>81</sup> and external magnetic field-assisted methods.<sup>157</sup>

Guo *et al.* first reported the *in-situ* template-assisted fabrication method.<sup>81</sup> They used air, glass and a specific solvent (pentanol) as templates to produce grooved surface hydrogel (G-SH), flat surface hydrogel (F-SH) and sharply dimpled surface hydrogel (D-SH), respectively. Commercially available AC paper was used as substrate and solar absorber, and a transparent PVA hydrogel layer was then prepared on the substrate to prepare a composite solar steam generator. As seen from the SEM images, G-SH has a rough surface with shallow holes (Figure 5A and 5B), but a higher magnification image (Figure 5C) reveals a relatively smooth sheet structure; F-SH tells a reasonably smooth outermost surface that is decorated with very shallow holes (Figure 5D) and shows a similar sheet-like structure at higher magnification (Figure 5E and 5F). For the D-SH sample, distinct "canyons" could be seen, resulting in a strongly dimpled surface topography (Figure 5G). The porous structures are strewn through canyon clusters (Figure 5H). Furthermore, D-SH has nanoscale pores nested in its micro-sized porous structure (Figure 5I), which neither G-SH nor F-SH has. D-SH has the highest RMS roughness with a surface area about 5 times that of its shadow area (Figure 5K). As a result, D-SH also shows super-oleophobicity (Figure 5J, OCA ≥ 150°), indicating that the super-wettability of PVA can be further tweaked by

increasing surface roughness. Due to the roughest surface, the most significant evaporation interface and the highest

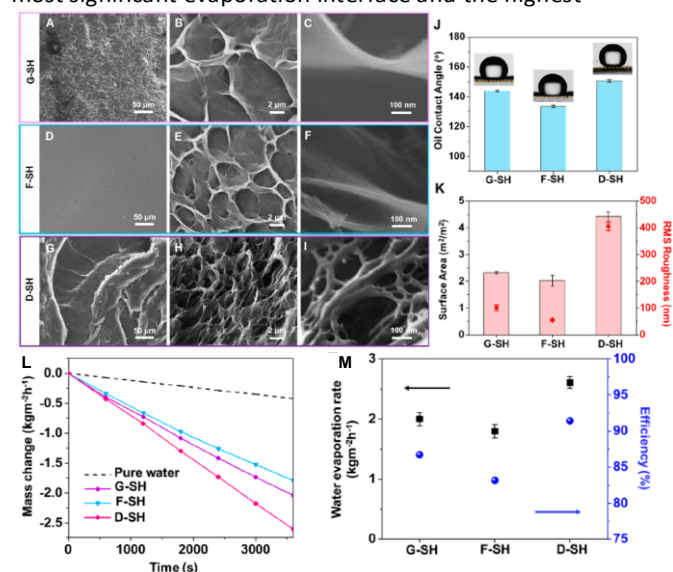


Figure 5. SEM images of different surface topography: (A–C) G-SH, (D–F) F-SH and (G–I) D-SH. (J) The underwater oil (1,2-dichloroethane) contact angle of each modified surface. (K) The optical profilometer test results revealed the surface area and root-mean-square (RMS) roughness of each sample. (L) The water mass changes, (M) water evaporation rates and energy conversion efficiencies of different samples under 1 sun. Reproduced with permission.<sup>81</sup> Copyright 2019, American Chemical Society.

hydrophilicity, D-SH displays the best SVG performance (Figure 5L and 5M) with a water evaporation rate of 2.6 kg m<sup>-2</sup> h<sup>-1</sup> and an energy conversion efficiency of *ca.* 91%.

The other novel surface modified method is only effective for solar absorber particles with magnetism, such as the Ni@RF@SiO<sub>2</sub> core-shell nanoparticles in Yang et al.'s work.<sup>157</sup> The nickel in the center of the core-shell structure is the source of magnetism (Figure 6g). The method primarily involves applying an external magnetic field to the magnetic solar absorber in order to adjust their distribution and convexity on the polymer surface, thus altering the surface morphology. In Figure 6, M-20, M-30 and M-40 represent composite membranes with particle concentrations of 20, 30, and 40 wt%, respectively. From the SEM images (Figures 6a–6d and 6h–6k), the number and height of surface microstructures increase in proportion to the strength of magnetic fields and the population of magnetic particles. As a result, M-40 has the most rough surface due to the highest external magnetic field and highest solar absorbers concentration, showing the best solar-driven steam generation performance of 2.25 kg m<sup>-2</sup> h<sup>-1</sup> at 95% energy conversion efficiency (Figures 6e and 6f).

Increasing the surface roughness of the hydrogel can simultaneously improve the light harvesting competence, and the effective evaporation surface area, which is beneficial to increase the production and energy conversion efficiency of the interfacial evaporator device. In contrast, the template-assisted surface construction method is more general, and suitable

templates can be used for various polymers for further development, while the method based on an external magnetic

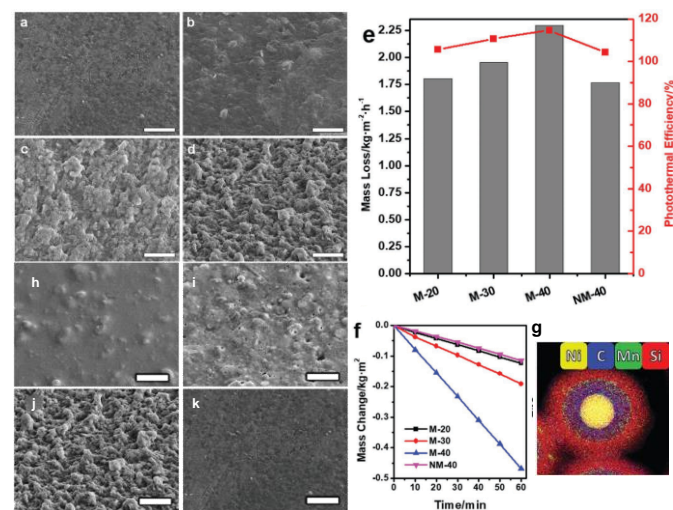


Figure 6. SEM images of Ni<sub>40</sub>C<sub>20</sub>/PVA composite film, with (a) 0 mT, (b) 100 mT, (c) 200 mT and (d) 400 mT magnetic field applied during gelation process as well as SEM images of (h) M-20, (i) M-30, (j) M-40 and (k) NM-40. (scale bar = 50  $\mu$ m) (e) The evaporation rates and energy conversion efficiencies of different films. (f) Water mass changes over time without light illumination at 20  $^{\circ}$ C on various films. (g) EDX mapping image of Ni@RF@SiO<sub>2</sub> core-shell nanoparticles. Reproduced with permission.<sup>157</sup> Copyright 2021, John Wiley and Sons. field is only ideal for magnetic solar absorbing particles, which has certain limitations.

### 2.3 Reducing heat loss

Aside from selecting the right solar absorber and tailoring surface topography, minimizing heat loss to the atmosphere and/or the bulk water is another effective way to boost solar-thermal conversion efficiency and overall water purification output. In principle, heat loss occurs in three ways,<sup>157</sup> including the thermal radiation of the platform, convection between the platform and the ambient air, and heat conduction from the surface to bulk water, which are all directly linked to the temperature of the platform or bulk water. Therefore, the surface or bulk water temperature is a critical reference value for measuring the heat loss of the platform. Current methods to reduce heat loss primarily rely on changing the distribution of solar absorbers,<sup>27, 33, 71, 73, 81, 98, 110, 139</sup> and incorporating heat-insulating materials.

As for the distribution of solar absorbers, uniform distribution of solar absorbers in the hydrogel matrix can reduce the heat flow inside the entire platform, thereby reducing heat loss compared to an unevenly dispersed system. For instance, the simply carboxylation treated CNTs can be uniformly distributed in the PAM matrix, improving energy conversion efficiency.<sup>27</sup> However, the even distribution of solar absorbers cannot mitigate heat dissipation to the surrounding environment. Therefore, researchers have designed multi-layered structures with all solar absorbers in a thin top layer to confine the energy around the evaporation interface.<sup>71, 73, 81, 98,</sup>

<sup>110, 139</sup> On this basis, Guo et al.<sup>33</sup> have developed a 'top-thin-layer' with magnetic-driven solar absorbers to further reduce the interface contact heat loss between different layers. In this

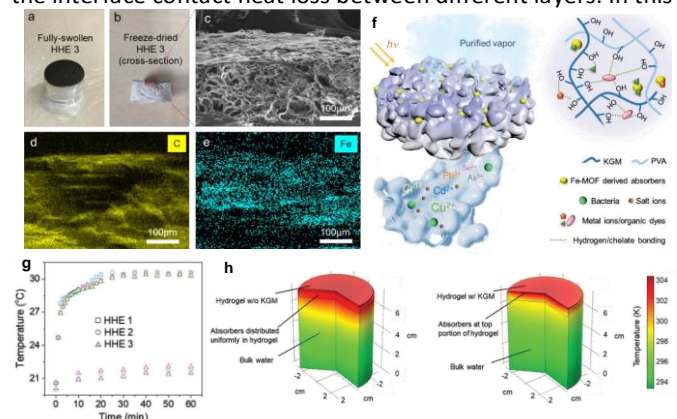


Figure 7. Spatial distribution of absorbers in HHE 3. Photographs of (a) fully swollen HHE 3; (b) cross-section of freeze-dried HHE 3; (c) SEM image of the top portion of HHE 3; the corresponding EDS mappings of (d) C and (e) iron elements. (f) Schematic illustration of solar water purification using HHEs. (g) Under 1 sun irradiation, the temperatures at both the hydrogel evaporator surface and in the bulk water. (h) COMSOL simulation results of the temperature distribution of a control sample (pure PVA hydrogel with uniformly distributed absorbers) and HHE 3. Reproduced with permission.<sup>33</sup> Copyright 2020, John Wiley and Sons.

work, they use a magnet to carry the iron-based metal-organic framework (Fe-MOF) derived solar absorber particles to one side of the PVA/konjac glucomannan (KGM, which also improves the heat insulation capacity) hydrogel to form a layered hybrid hydrogel evaporator (HHE, Figure 7f). HHE 3 with a KGM/PVA weight ratio of 0.16:10 shows the highest evaporation rate (3.2 kg m<sup>-2</sup> h<sup>-1</sup>) at the highest energy conversion efficiency (90%). As seen from Figures 7a-7c, the black solar absorbers are located at the top of HHE 3, which is also confirmed by the EDS mapping (Figures 7d-7e). The surface temperature and bulk water temperature reach equilibrium temperatures of 31 and 22  $^{\circ}$ C, as shown in Figure 7g. According to the COMSOL simulation results (Figure 7h), HHE 3 can keep heat close to the evaporation surface to reduce heat loss. This study thus proved its higher energy conversion efficiency compared with the evaporator with evenly distributed solar absorbers. In addition, there are some other methods to confine the solar absorbers on the surface layer, such as using the difference in surface tension between ethanol and water,<sup>132</sup> concentrating them on one end of the hydrogel under gravity,<sup>80</sup> carbonized the upper side of the hydrogel,<sup>88, 159</sup> and so on.

For heat management, in addition to using the solar absorbers as the heat-generating phase, the other phase in the platform usually exists as heat insulating substances. Hydrogels with high water content have inherent heat insulation ability. To further enhance the overall heat insulation, most studies add a heat insulation layer, such as PSS,<sup>101</sup> PS,<sup>85, 137</sup> PE,<sup>76, 77</sup> EPE,<sup>90</sup> TE<sup>123</sup> foam and so on, at the bottom of the evaporation platform. Yet, recent research incorporated heat confinement components such as specific aerogel spheres<sup>32</sup> and hydrophobic

associations<sup>27</sup> into the hydrogels to lift their overall heat insulation performance. Tan *et al.*<sup>32</sup> controlled the gelation

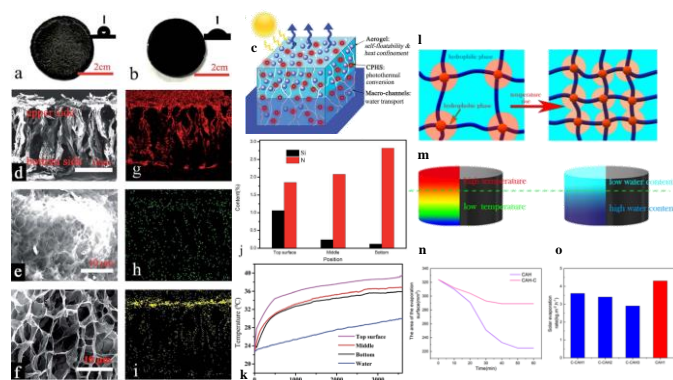


Figure 8. Photos of the (a) upper and (b) bottom surface of the CPHS/aerogel functionalized hydrogel, and the inset is the contact angle image. (c) Solar steam generation schematic based on functional hybrid hydrogels. SEM images of (d) cross-section of the hydrogel, (e) upper and (f) bottom surface of the hydrogel; EDS mapping of (g) C, (h) N and (i) Si. (j) Si and N contents of different parts from EDS. (k) Under 1 sun, temperature–time plots of various sections of the hydrogel and bulk water. Reproduced with permission.<sup>32</sup> Copyright 2019, Royal Society of Chemistry. Schematic illustration of (l) the composition of a hydrophobic association hydrogel's microphase separation and the structural change caused by temperature; And (m) the correlation between the temperature distribution and the water content in the hydrophobic association hydrogel. (n) Change in the CAH's and C-CAH's evaporation surface area. (o) C-CAHs' evaporation rates. Reproduced with permission.<sup>27</sup> Copyright 2020, American Chemical Society.

conditions and prepared poly(aniline-co-pyrrole) hollow spheres/PVA hybrid hydrogel with gradient distribution of silica aerogel particles (Figure 8c). The resultant hydrogel has a hydrophobic rough upper surface and a smooth hydrophilic bottom surface (Figures 8a–8b). The EDS mapping result confirmed the gradient distribution (Figures 8g–8i) and the element's contents analysis in different parts (Figure 8j). As a result, the upper part of the hydrogel has lower thermal conduction ( $0.2 \text{ W m}^{-1} \text{ K}$ ) than that of the bottom part ( $0.54 \text{ W m}^{-1} \text{ K}$ ), resulting in higher temperature variations in the top surface than bulk water (Figure 8k). Zhang *et al.*<sup>27</sup> used hydrophobic lauryl methyl acrylate (LMA) micelles as cross-linkers to construct hydrophobic associations in a PAM hydrogel. As shown in Figure 8l, the hydrophobic and hydrophilic phases were coexisting in the hydrogel, resulting in isolated micropores. If the temperature of the hydrogel rises, the interaction between molecular chains and water molecules weakens, resulting in a decrease in the water content of hydrogel. Due to the higher temperature at the top of the hydrogel, there is less water around the evaporation interface (Figure 8m), reducing heat loss from the top surface caused by excess water. A control hydrogel sample was prepared to demonstrate this speciality by omitting the hydrophobic

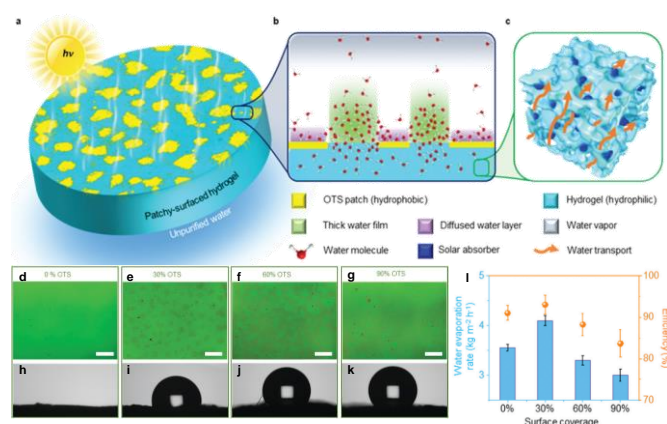
association (C-CAH). This sample showed slower shrinkage and larger evaporation surface area than CAH (Figure 8n). As a result, with less heat loss, the evaporation rate of hydrophobic association hydrogel is higher than that of C-CAHs (Figure 8o). More recently, Wu *et al.*<sup>160</sup> reported a multi-layer spherical evaporator composed of a PS core and multi-layer outer coatings (PS-cellulose-PDA-PPy-PDA). This design reduces its density and restricts water transport only through the outer hydrophilic layers. Only a small part of the water can contact the water, thereby limiting the heat loss from the evaporation surface to the bulk water. In all, hydrophobic ingredients have been proven to be thermal confinement components to reduce heat loss.

### 3. Enhancing water transport/activation capacity

Water management, including water transport and water activation, is another critical process that determines the overall performance of solar water purification. Fast water transport speed can ensure continuous water supply to the evaporation interface. Adjusting the wettability and tuning the internal water transport channels are the two main design principles to enhance water transport. In addition, the capacity of the platform to promote water activation is essential to decrease the water vaporization enthalpy to improve the energy conversion efficiency and the evaporation rate (see Equ (1) in section 2).

#### 3.1 Adjusting the wettability

A practical method is to reduce the surface wettability to improve the water transport competence. Examples include using hydrophobic polydimethylsiloxane (PDMS) as the top layer,<sup>121</sup> adding hydrophobic Si aerogels mainly in the upper part,<sup>32, 102, 161</sup> selectively decorating the upper surface with PFOTS<sup>159</sup> and reducing hydrophilic GO into hydrophobic rGO at the top side via laser.<sup>162</sup> Furthermore, Guo *et al.*<sup>34</sup> have reported



a patchy surface with hydrophobic and hydrophilic parts for Figure 9. (a–c) Schematic illustration of patchy-surface hydrogels (PSHs). (d–k) Optical images and contact angles of PSHs with (d and h) 0%, (e and i) 30%, (f and j) 60%, and (g and k) 90% OTS covered surfaces. The scale bars are all 20 mm. (l) PSHs' evaporation rates and corresponding energy conversion



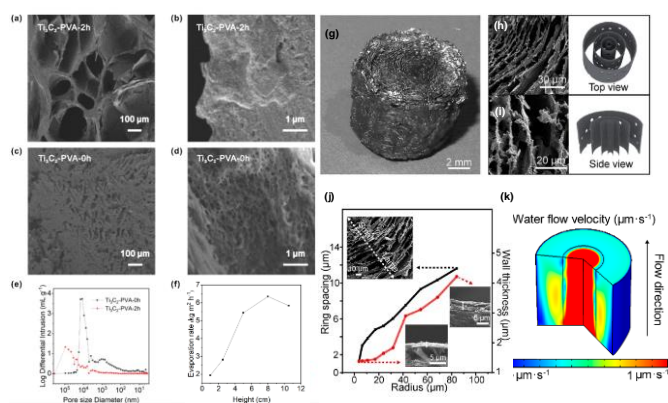
efficiencies under 1 sun. Reproduced with permission.<sup>34</sup> Copyright 2020, Royal Society of Chemistry.

higher water transport speed and excellent SVG performance ( $4 \text{ kg m}^{-2} \text{ h}^{-1}$  with 93% energy conversion efficiency Figure 9). The hydrogel has a partial trichloro(octadecyl)silane (OTS) modified surface, with the island-shaped patches being hydrophobic and the rest being hydrophilic (Figure 9a). The thickness of the water film increased as a large portion of the water is confined in the hydrophilic region; thus, the effect of hydrogel surface on the outmost water molecules is decreased, resulting in faster evaporation (Figure 9b). The optical images and increasing water contact angles confirm the successful OTS modification of the surface of the hydrogels (Figure 9d-9k). Moreover, the introduction of hydrophobic components into the hydrogels can lead to the formation of internal gaps, thus ensuring rapid water replenishment.<sup>27</sup>

### 3.2 Tuning internal water channels

The internal water channel is a vital channel for rapid water transport that can be constructed from three perspectives: size,<sup>51, 84, 114</sup> direction,<sup>46, 62, 97, 122, 163</sup> and structure<sup>164</sup> to enhance the pumping force and/or capillary effect.

To tune the size of the water channel, Liang *et al.* have put forward a simple and fast construction method via fermentation. However, the evaporation rate is not high enough ( $1.611 \text{ kg m}^{-2} \text{ h}^{-1}$ ) due to the large pores formed ( $900\text{--}2,540 \mu\text{m}$ ).<sup>84</sup> Li *et al.*<sup>51</sup> used the ice-template method to narrow the size of inner channel sizes to the submicrometer range, inducing a strong capillary force to achieve rapid water transport over a long distance. The pore structures and size distribution are shown in Figures 10a-10e, and the highest evaporation rate is  $6.35 \text{ kg m}^{-2} \text{ h}^{-1}$  over a long transport distance of 8 cm (Figure 10f). In addition to the uniform size channel, Meng *et al.*<sup>114</sup> proposed an N-doped rGO aerogel with ring-like gradient vertically aligned microchannels as shown in Figure



10g.

Figure 10. (a-d) SEM images of  $\text{Ti}_3\text{C}_2\text{-PVA-2h}$  and  $\text{Ti}_3\text{C}_2\text{-PVA-0h}$ . (e) Pore size distribution. (f) The evaporation rates and the corresponding maximum water transport height. Reproduced with permission.<sup>51</sup> Copyright 2020, American Chemical Society. (g) Photo of the N-RGO aerogel with ring-like architecture. The SEM images and corresponding schemes from (h) the top and (i) side view. (j) From the middle to the edge, the wall thickness and spacing increase. (k) Simulation of the ring-like aerogel's water flow velocity with gradient microchannels, suggesting

concentrated pumping in the middle. Reproduced with permission.<sup>114</sup> Copyright 2020, American Chemical Society.

From Figures 10h-10j, it is found that the spacing and wall thickness increase from the center to the edge, and the specific channel sizes distribution is realized by introducing a concentration gradient of  $\text{NH}_4\text{OH}$  (as antifreeze) before freeze-drying. The gradient channel size distribution can ensure concentrated pumping in the center, as reflected by the simulation results in Figure 10k, leading to a high evaporation rate of  $2.53 \text{ kg m}^{-2} \text{ h}^{-1}$ .

Inspired by the water transport in the trees in nature, vertically aligned internal channels have the potential to quickly transport water from the bottom of the evaporation generator to the top and release vapor quickly (Figure 11a). The direction freezing method<sup>62, 97</sup> is usually used to construct vertically aligned channels. For example, Yu *et al.*<sup>62</sup> prepared a PVA/MXene hydrogel with wood-like vertically aligned channels using the above method (Figure 11b). The hydrogel with vertically aligned channels (TIH3) represents higher water mass change than that of bulk water, MXene membrane (MM) and non-tree-inspired hydrogel (n-TIH3) (Figure 11c). As a result, the TIH3 shows a high evaporation rate of  $2.71 \text{ kg m}^{-2} \text{ h}^{-1}$  at 90.7% energy conversion efficiency as a vapor generator in solar water purification. Besides, the tortuosity of the internal channels can be adjusted by introducing chitosan (CTS) content in the hydrogels.<sup>46, 163</sup> With a higher content of CTS, lower-tortuosity channels can be achieved to speed the water transport as well as lift the evaporation rate and energy conversion efficiency (Figure 11d). Xu *et al.* have proposed a radial ice-template method (Figure 11g) to achieve the radial vertically-aligned channels, which are more similar to the internal channels of a tree (Figure 11e).<sup>122</sup> The aerogel with radial vertically-aligned channels shows stronger water transport capacity over a longer

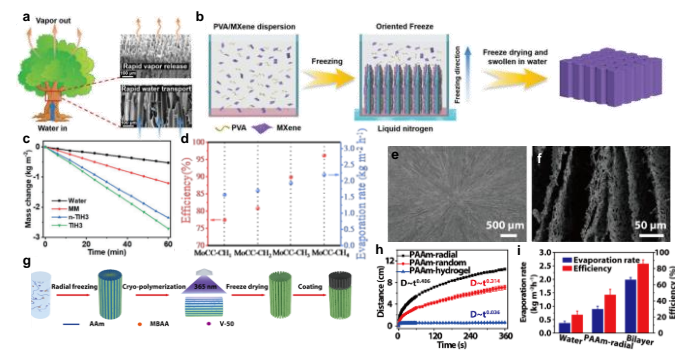


Figure 11. (a) Schematic illustration of the water transport in tree from root to the top with the SEM images of the top and bottom of wood. (b) Schematic illustration of the direction freezing method. (c) Water mass loss for pure water, MM, n-TIH3, and TIH3 under 1 sun. Reproduced with permission.<sup>62</sup> Copyright 2020, John Wiley and Sons. (d) Evaporation rates and energy conversion efficiencies of MoCC-CHs. Reproduced with permission.<sup>163</sup> Copyright 2020, American Chemical Society. (e-f) SEM images of radially aligned channels and micropores. (g) Schematic illustration of the radial freezing method. (h) Water transport distance over time. (i) Water evaporation rate and energy conversion efficiency of PAAm-based aerogels with



different channel directions. Reproduced with permission.<sup>122</sup> Copyright 2019, American Chemical Society.

distance than others (Figure 11h), but it displays a medium SVG performance with an evaporation rate of  $2 \text{ kg m}^{-2} \text{ h}^{-1}$  at 85.7 % energy conversion efficiency (Figure 11i). This is relatively lower than the hydrogels with vertically aligned channels.

Gradient capillarity has been proved to facilitate strong direction-limited water transport (Figure 12b) in hydrogels. Liang *et al.*<sup>164</sup> developed an effective fabrication method based on the G-T template to fabricate gradient structure hydrogels (Figure 12a), in which G represents glass while T represents polytetrafluoroethylene (PTFE). From Figure 12b, it is found that between the top and bottom of the gradient-structured hydrogel, the sizes of the channel is changing continuously. The improved capillary pumping through the channels from the bottom in water to the surface in air results in rapid, one-way water replenishment, allowing for a high evaporation rate ( $1.684 \text{ kg m}^{-2} \text{ h}^{-1}$  at 93.4 % energy conversion efficiency) and less heat loss. The optical photos and SEM images of the G side and T side reveal a considerable difference in the size of the different side channels (Figures 12c-12e).

### 3.3 Water activation

Specific water states in polymer hydrogels can make the water more active, thereby facilitating the evaporation process. Water behaves differently inside hydrogels because the hydrophilic polymer chains have a distinct preference for water molecules, which is reflected in intermolecular hydrogen bonds of different strengths. Three forms of water have been identified in the hydrated polymer network, including bond water (BW, dark blue color area in Figures 13a-13b) with water-polymer bonding, free water (FW, light blue color area) with water-water bonding, and intermediate water (IW, yellow color area) with weakened water-polymer and water-water bonding between BW and FW. IW is the key water state which requires less energy to escape from the adjacent molecules to decrease the water evaporation enthalpy, realizing higher energy conversion efficiency (according to Equ 1). Therefore, in order to reduce the energy demand for water evaporation from the hydrogel, it is desirable to tune the building blocks to achieve a higher amount of IW within hydrogels.

Considerable efforts have been devoted to tuning the IW content in hydrogel networks, including the adjustment of polymer concentration, the introduction of hydrophilic

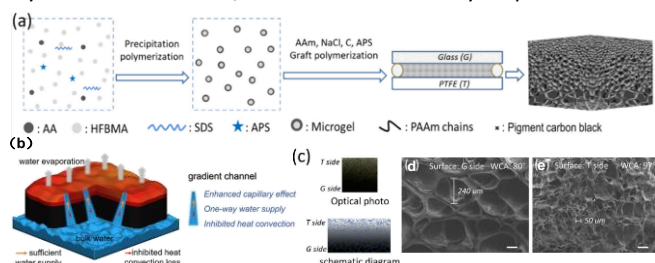


Figure 12. (a) Fabrication process of gradient structured hydrogel via G-T template method. (b) Schematic illustration of gradient structured hydrogel-based solar vapor generation. (c) Optical photo and schematic diagram of gradient structure.

SEM images of the (d) G and (e) T side. Reproduced with permission.<sup>164</sup> Copyright 2020, Elsevier.

functional groups ( $-\text{OH}$ ,  $-\text{COOH}$ ,  $-\text{SO}_3\text{H}$ ,  $-\text{NH}_2$  and  $-\text{CONH}-$ , to form noncovalent interaction), the change of cross-linking density, and the construction of porous structures.<sup>165</sup> For example, Zhou *et al.*<sup>135</sup> tuned the PVA/CTS ratios from 1:0 to 1:0.25 to form hydrogels, namely h-LAH1-5. Their IW/FW ratios increased, and the equivalent vaporization enthalpy decreased correspondingly, as shown in Figures 13c-13d. However, the evaporation enthalpy is not the only factor that can influence the water evaporation performance. h-LAH5, which has the lowest vaporization enthalpy, still has a high water content, which hinders effective energy utilization and restricts evaporation rate. After balancing these two factors, h-LAH4 with a relatively higher water vaporization enthalpy and relatively lower water content shows the highest evaporation rate of  $3.6 \text{ kg m}^{-2} \text{ h}^{-1}$  and the best energy conversion efficiency of 92%.

In addition, ionic polymers have electrostatic interaction with water molecules, stronger than hydrogen bonding between polymer chains and water molecules. Zhou *et al.*<sup>82</sup> incorporated polystyrene sulfonate (PSS), which can be hydrated with water via electrostatic interaction and hydrogen bonding, into the PVA networks to form a semi-interpenetrating polymer networks gel (IPNG, Figure 13f). IPNG1-5 have different PSS/PVA ratios of 0:1, 1:1, 1.5:1, 2:1 and 1:0, and their IW/FW ratios can be calculated from the differential scanning calorimetry (DSC) curves (Figure 13e). It is found that with the increase of PSS content, the ratio of IW/FW increases in response, mainly due to the increase of IW. However, when the

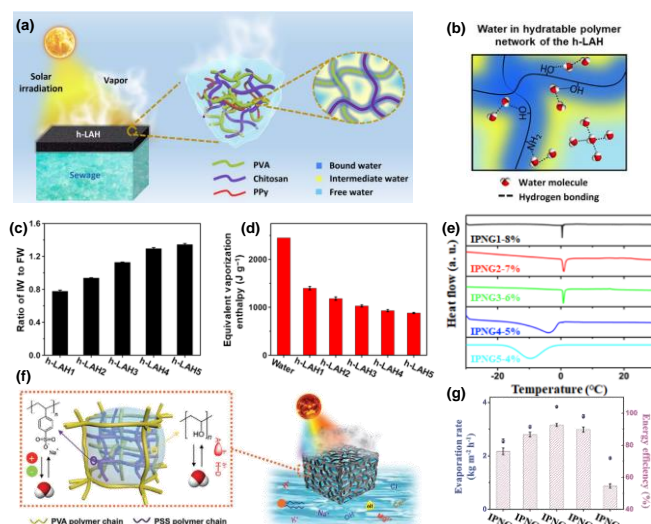


Figure 13. (a) Schematic illustration of solar vapor generation based on h-LAH. (b) Water state in h-LAH. (c) In h-LAHs, the IW/FW ratio. (d) Bulk water and the water in h-LAHs' equivalent water vaporization enthalpy. Reproduced with permission.<sup>135</sup> Copyright 2019, American Association for the Advancement of Science. (e) The melting activity of IW in various frozen IPNGs as depicted by DSC curves. (f) Solar water purification with controlled hydration based on IPNG. (g) IPNGs' solar evaporation rate and energy conversion efficiency under 1 sun.

Reproduced with permission.<sup>82</sup> Copyright 2020, John Wiley and Sons.

IW content reaches the maximum limit, the ratio will drop simply because FW content will continue to increase. As a result, IPNG3 with a PSS/PVA ratio of 1.5:1 shows the highest IW/FW ratio and the highest evaporation rate ( $3.86 \text{ kg m}^{-2} \text{ h}^{-1}$ ) with an energy conversion efficiency of 92% (Figure 13g).

In addition to the aforementioned methods, some recent researches also use polyelectrolyte-based hydrogels as well as some other strategies to implement strong ionic pumping,<sup>83</sup> construct an overall water management system<sup>54, 151, 166</sup> and stimulate water transport and evaporation.

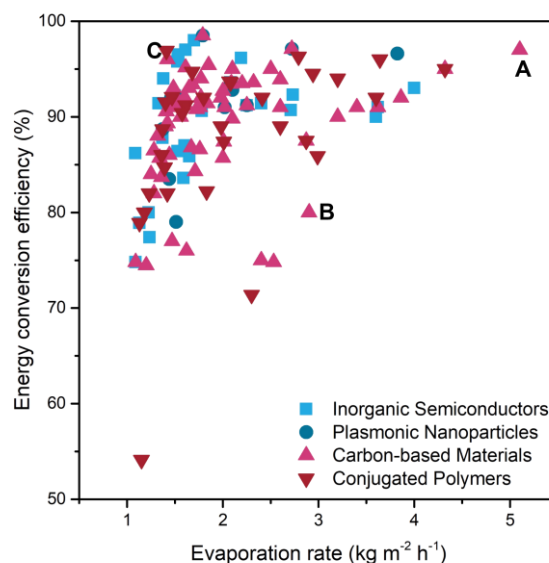
#### 4. Future research roadmap

Based on these main design principles, the solar water purification system still has many areas that can be further improved and strengthened to cope with practical water purification issues.

First of all, as shown in **Figure 14** and **Table 1**, it is still a challenge to achieve a reasonably high evaporation rate and energy conversion efficiency at the same time (For fair comparison, studies with energy conversion efficiency >100% are not included). Taking solar water purification with CNTs as solar absorbers as an example, point B<sup>124</sup> represents the two-layered biomimetic CNTs/bacterial cellulose hydrogel reported by Guan *et al.* It shows a high evaporation rate close to  $3 \text{ kg m}^{-2} \text{ h}^{-1}$ , but the energy conversion efficiency is only about 80%. In contrast, Zhou *et al.* (point C)<sup>125</sup> proposed a 3D pillared CNTs/PAM hydrogel with selected hydrophobic modification, which has relatively high energy conversion efficiency (96%), yet low evaporation rate ( $1.42 \text{ kg m}^{-2} \text{ h}^{-1}$ ). In a separate design strategy, most materials only have good performance in limited aspects, but the coordinated design in multiple aspects can bring better and more comprehensive performance. For instance, in a recent study of carboxyl CNTs/PAM composite hydrogels reported by Zhang *et al.*<sup>27</sup> (point A), the resulting system exhibited the highest evaporation rate ( $5.1 \text{ kg m}^{-2} \text{ h}^{-1}$ ) as well as excellent energy conversion efficiency (97%). This result can be attributed to the use of hydrophobic association in the skeleton and double-layer structure of carbon nanotubes only in the top layer to achieve lower energy loss and ultra-fast water replenishment. Therefore, on the basis of complying with these design principles, the entire preparation process should be coordinated with each other from the perspectives of chemistry, materials and engineering to maximize the evaporation rate and energy conversion efficiency at the same time.

Since this technique utilizes the most abundant and inexhaustible renewable energy source, which is friendly for developing countries and poverty-stricken areas, lower capital and operating costs will make it more competitive. Using biochar or biomass-derived solar absorbers<sup>91-93, 167</sup> are regular cost-reducing strategy because the raw materials can be obtained from nature. A research group even coated PPY on the real *setaria viridis* spike to use the plant's own water transport and evaporation-promoting properties to maximize its

potential.<sup>142</sup> Other studies have reported the use of specific solid waste as solar absorbers, including red mud (residue of the industry of aluminum mining),<sup>168</sup> semi-coke,<sup>169</sup> and pencil



graphite.<sup>170</sup> Besides, reducing the use of solar absorbers by Figure 14. The diagram summarises the solar water purification performance of different systems. Data acquired from ref.<sup>24-27, 32-34, 40-43, 46-67, 71-128, 130-132, 135-151, 153-164, 166-181</sup> (All the studies in this figure are under the solar intensity of 1 sun. Studies with energy conversion efficiency >100% are not included for fair comparison).

distributing them only around the evaporation interface<sup>33, 146</sup> and constructing multilayer-structure with only one layer of them<sup>71, 73, 81, 94, 98, 139</sup> is also effective. Moreover, designing a recyclable solar water purification platform<sup>[28, 104]</sup> is another proven solution.

In practical application, better anti-fouling performance can guarantee long-term operation, divided into anti-biofouling and crystalline anti-fouling. The anti-bacterial performance can be achieved by adding CTS.<sup>41, 110</sup> Guo *et al.*<sup>181</sup> recently attached catechol groups to the CTS hydrogel for hydrogen peroxide (a broad-acting bacterial-killing agent) generation, combining with the synergy effect of quione-modified AC, to enhance the anti-fouling property and guarantee 3 months of performance maintenance. There are numerous methods to improve the anti-crystalline fouling ability, including the construction of the Janus structure<sup>128, 162</sup> and the umbrella-shaped platform,<sup>89</sup> the use of ions rejection polymer,<sup>83, 150, 166</sup> the introduction of bubbles in the middle section,<sup>138</sup> the weight imbalance sensitive spherical platform capable of rotating and renewing the evaporation surface,<sup>160</sup> the millineedle array on the surface for site-specific salt crystallization without salt clogging<sup>153</sup> and so on. In addition, the self-floating hydrogel platform is out of external support substrate, which is not conducive to water transport, usually by adding low-density materials (*i.e.* Si aerogels)<sup>32</sup> or preparing a partially hydrophobic bottom layer.<sup>138</sup>

Drawing inspiration from existing organisms on the planet is another effective strategy to improve solar water purification performance. The most common is to imitate the water absorption of the roots of plants and the water evaporation of the leaves to enhance the water transport process.<sup>62, 97</sup> Inspired from the porifera in the sea, Wang *et al.*<sup>178</sup> fabricated a hydrogel platform with the sponge as a skeleton and the black hydrogel as skin, which could be arbitrarily compacted, folded, and twisted as well as stayed stable for more than 6 months in different environments. What's more, imitating the water absorption and release cycle of pufferfish, the inherent lower critical temperature of poly(*N*-isopropyl acrylamide) (PNIPAm) hydrogel was used for hydrophilic (in dark conditions) and hydrophobic (under sunlight) conversion.<sup>152</sup> Additionally, surface biomimetic morphology is also common in studies to enhance light acquisition,<sup>67, 87</sup> anti-fouling,<sup>153</sup> and additional water collection capacity.<sup>144</sup>

In addition to seawater desalination and wastewater purification, there are still some other particular application scenarios for solar water purification. The recent news that Japan intends to dump nuclear wastewater into the ocean has sparked international concern. Some research groups proposed using solar water purification to purify radioactive wastewater<sup>116</sup> and recover radioactive elements, e.g. uranium.<sup>120, 126, 156</sup> Besides, the application of this technology to purify specific wastewater containing nanoparticles,<sup>137</sup> acidic,<sup>174</sup> alkaline,<sup>92</sup> low-boiling-point contaminants,<sup>177</sup> and organic dyes<sup>142, 154</sup> are also under development. Furthermore, additional functions, such as electricity generation,<sup>49, 86, 99, 123, 125, 127, 136</sup> fog collection,<sup>144</sup> oil/water separation,<sup>145</sup> water disinfection,<sup>181</sup> sensing,<sup>56</sup> and photo degradability,<sup>63, 78</sup> have also been integrated into solar water purification.

**Table 1.** Different solar water purification systems proposed in recent years and related performance.

Ref.	Year	Material	Energy concentrating	Water transport/activation	Solar intensity (sun)	Evaporation rate (kg m <sup>-2</sup> h <sup>-1</sup> )	Energy conversion efficiency
<sup>25</sup>	2018	PVA/PPy hierarchically nanostructured hydrogel	PPy	PVA internal channels and IW generation	1	3.2	94.00%
<sup>100</sup>	2018	PVA/rGO hybrid hydrophobic hydrogel	rGO	osmotic swelling and capillary channels	1	2.5	95.00%
<sup>147</sup>	2018	Macroporous PEGDA-PANi double-network hydrogel	PANi nanowires, porous surface and 2d device heat insulation	capillary force of cellulose in 2D device	1	1.4	91.50%
<sup>101</sup>	2018	Highly vertically ordered pillar array of graphene-assembled framework	rGO+heat insulation device (PSS)	hydrophilic cotton bars for wicking water	1	2.1	95.00%
<sup>90</sup>	2018	Carbonized wood/EPE foam/hydrophilic airlaid paper	Black carbonized wood and EPE foam thermal insulation	hydrophilic airlaid paper and imitating the water transport and transpiration of tree	1	1.45	91.30%
<sup>81</sup>	2019	2-layered hydrogel with PVA surface modified	AC paper at bottom and sharply dimpled surface	PVA internal channels and IW generation	1	2.6	91.00%



			hydrogel/AC paper				
24	2019	PVA/TiO <sub>2</sub> sponge-like hydrogel	TiO <sub>2</sub>	3D interconnected porous structure	1	3.6	90.00%
135	2019	PPy/PVA/CTS hydratable hydrogel	PPy	Hydratable -IW generation	1	3.6	92.00%
85	2019	Melamine-derived carbon sponges	melamine-derived carbon sponges and PS as thermal insulator	air-laid paper	1	1.98	92.00%
131	2019	C dots/CTS/carboxymethyl cellulose hydrogel	C dots		1	1.4	89.00%
57	2019	Protonated g-C <sub>3</sub> N <sub>4</sub> /graphene hybrid hydrogel	GO and g-C <sub>3</sub> N <sub>4</sub>		1	1.09	74.8%
76	2019	CuS/macroporous PAM	CuS, rough surface of PAM and PE as thermal insulator	PE foam wrapped in cotton cloth	1	1.46	92% (87.5% after 50 cycles)
40	2019	Mesoporous cellulose/TiO <sub>2</sub> /SiO <sub>2</sub> /TiN hydrogel	TiO <sub>2</sub> , SiO <sub>2</sub> , TiN and low thermal conductivity		1	1.235	77.39%
71	2019	Double-layer Ag-PSS-agarose gel/agarose gel	Ag NPs (LSPR effect)		1	2.1	92.80%
32	2019	Poly(anilineco-pyrrole) hollow spheres/Si aerogel microparticals/PVA	Poly(anilineco-pyrrole) hollow spheres and Si aerogel microparticals	Upper hydrophobic and bottom hydrophilic Janus surface (gradient distribution of Si)	1	1.83	82.20%
59	2019	Mo <sub>2</sub> C+PVA hydrogel	β-Mo <sub>2</sub> C (Mxenes, semiconductor)		1	1.59	83.60%
83	2019	AC foam/P(SA) polyelectrolyte foam hydrogel	AC foam	Ionic pumping (better than capillary)	1	1.3	

				pumping, fouling rejection; thicker for thermal insulation and high flux)			
102	2019	GO/Si aerogel/PAM/ PVA composite hydrogel	GO nanosheets	Upper hydrophob ic and bottom hydrophilic	2	2.696	
96	2019	PVA or PU or melamine and CB NPs	CB NPs		1	2.15 for PVA based	
108	2019	rGO/PAM hybrid mushroom-like cryogel	rGO		1	1.76	86.60%
109	2019	N-doped graphene /carbon hybrid aerogels	N-doped graphene /carbon		1	1.558	90.00%
139	2019	PPy coating pre-pressed MF and pre- pressed MF 2 layered hydrogel	PPy		1	1.574	90.40%
172	2019	Flame-treated melamine foam (F-MF) assembled with expanding polyethylene (EPE) foam	F-MF		1	1.18	80.00%
140	2019	Large-area polypyrrole chemically functionalized cellulose paper (PPyP)	PPy		1	2.99	85.89%
48	2019	Ni foam loading Co <sub>3</sub> O <sub>4</sub> with nanoscale superstructure s	Co <sub>3</sub> O <sub>4</sub>		1	1.226	80.00%
141	2019	PPy/FexOy/CTS nanostructure d gel membrane	PPy		1	1.93	
110	2019	2-layered hydrogel with GO aerogel and	GO		1	1.725	90.80%

		chitosan/ZnO composite layer					
122	2019	MWCNTs/PAA m aerogel	MWCNTs	Radially aligned channels via radial ice-template method for long-distance quick water transport	1	2	85.70%
42	2019	Cu/C/SiO <sub>2</sub> /TiO <sub>2</sub> hollow microparticles with thin shell	Cu/C/TiO <sub>2</sub> and SiO <sub>2</sub> as thermal insulation		1	1.5	92.20%
123	2019	CNT/cellulose nanocrystals nanocomposite and PDMS sponge	CNT/CNC nanocomposites and TE module as thermal insulator		1	2.01	87.40%
58	2019	Dual-phase MoN/Mo <sub>2</sub> N	dual-phase MoN/Mo <sub>2</sub> N		1	1.7	98.00%
111	2019	PVA/rGO hydrogel, MFfoam and $\beta$ -chitin	rGO	$\beta$ -chitin; Artificial Tree (184 cm)	1	1.6	
65	2019	copper-zinc-tin-selenide nanocarambol as assembled membrane	p-type CZTSe		1	1.528	86.40%
92	2019	Ethanol-treated-carrot biochar	Carrot biochar		1	2.04	127.80%
33	2020	KGM/Fe-MOFdAPs/PVA hybrid hydrogel	Fe-MOFdAPs (magnet-assisted, fewer solar absorbers) and KGM (heat insulation)	KGM for fast water transport and better hydration ability	1	3.2	90.00%
34	2020	PVA/OTS/Ti <sub>2</sub> O <sub>3</sub> patchy-surface hydrogel	Ti <sub>2</sub> O <sub>3</sub>	OTS (hydrophobic)+PVA (hydrophilic), faster evaporation	1	4	93.00%
82	2020	AC/PVA/PSS interpenetrating hydrogel	AC	PSS (electrostatic interaction)	1	3.86	92.00%



					with water molecules)			
60	2020	HxMoO <sub>3</sub> /PNIPAM hydrogel	HxMoO <sub>3</sub>		1	1.65	85.87%	
89	2020	Hydrophilic acrylamide polymer (resilience)/biochar particles/SDS sponge-like hydrogel	Rice husk biochar particles	Umbrella-shaped	1	1.77±0.05	94.00%	
98	2020	2-layered cellulose-based bottom hydrogel/cellulose-based CB hydrogel	CB		1	1.582	91.40%	
51	2020	Ti <sub>3</sub> C <sub>2</sub> or MoS <sub>2</sub> /PVA	Ti <sub>3</sub> C <sub>2</sub> or MoS <sub>2</sub> nanosheets	Adjust inner channel sizes through an ice-templating method	1	6.35		
61	2020	Vertically aligned rGO/Ti <sub>3</sub> C <sub>2</sub> Tx MXene hybrid hydrogel	rGO, Ti <sub>3</sub> C <sub>2</sub> Tx MXene sheets	Vertically aligned channels via directional-freezing technique	1	2.09	93.50%	
84	2020	AC/fermentation porous PVA hydrogel	AC	tune internal channel size for fast water transport via fermentation	1	1.611	95.15%	
164	2020	Gradient structured C/polyacrylamide (C/PAAm) composite hydrogel	C powder	Enhanced capillary pumping through the microchannels leads to rapid, direction-limited water replenishment	1	1.684	93.40%	

72	2020	rGO/Ag/sodium alginate (SA) hydrogel supported by a PU sponge	rGO and Ag nanowires	Super hydrophilic : swelling ability	1	2.02	91.00%
103	2020	Graphite nanosheets/SiO <sub>2</sub> /PVA/Fe <sub>3</sub> O <sub>4</sub> floating magnetic hydrogel	Graphite nanosheets	Semi-automatic fresh water collection device		1.196	
73	2020	2-layered hydrogel with PPy/Ag/PMBA-BrILs hydrogel as top layer and PMBA-BrILs hydrogel as bottom layer	PPy and Ag	Poly(ionic liquid)s for imidazolium-based cations and bromine anions reject ions	1	1.37	88.70%
167	2020	Squid ink/starch hydrogel	Squid ink		1	2.07	93.7%
163	2020	Molybdenum carbide/carbon-based chitosan hydrogel	MoCC sphere	low tortuosity channels (content of Chitosan)	1	2.19	96.15%
62	2020	Ti <sub>3</sub> C <sub>2</sub> T <sub>x</sub> /PVA tree-inspired hydrogel	Mxene Ti <sub>3</sub> C <sub>2</sub> T <sub>x</sub>	Vertically aligned channels via directional freezing technique	1	2.71	90.70%
27	2020	2-layered CNTs/PAM hydrogel	CNTs and hydrophobic association for less thermal loss	Hydrophobic and hydrophilic groups in hydrogel skeleton	1	5.1	97.00%
161	2020	Squid ink NPs/SA/PVA/PAM floatable composite hydrogel	Squid ink NPs	Physical and chemical cross-linking; top hydrophobic and bottom hydrophilic	4	2.3	71.38%
149	2020	Sodium alginate/PEDOT/PSS 3D hydrophilic network	PEDOT	Ionic hydrogel	1	1.23	82.00%

148	2020	PIC/PANI hierarchically porous hydrogel	PANI and PS foam as thermal insulation	PS foam	1	2.79	96.30%
104	2020	rGO hydrogel membrane	rGO		1	2.33	
55	2020	Fe-Mo <sub>2</sub> S <sub>3</sub> /sodium alginate starch hydrogel	Fe-Mo <sub>2</sub> S <sub>3</sub>		1	2.4	91.40%
112	2020	Modified graphene/coal oxide aerogels	Graphene/coal oxide		1	1.62	76.00%
113	2020	N-doped maize straw/GO aerogel	GO	Maize straw	1	3.22	
124	2020	CNTs/BC hydrogel with glass bubbles/BC hydrogel/wood substrate	CNTs and thermal insulation layer glass bubbles/BC	Wood substrate and 3D cellulose nanofiber network of the BC hydrogel	1	2.9	80.00%
91	2020	Carbonized loofah sponge and alkalized loofah sponge	Carbonized loofah sponge hydrogel and alkalized loofah sponge as thermal insulator		1	1.36	83.70%
49	2020	multilayered PDMS/CuO/Cu foil/PAM hydrogel	hierarchical micro–nano CuO, PAM for heat confinement and PDMS for impeding light escaping	PAM (water suction)	1	1.33	91.40%
114	2020	Porous N-doped rGO with gradient microchannels 3D aerogel	rGO	Gradient microchannels and N for improving the ability of water transport and evaporation	1	2.53	74.80%
75	2020	Porous Au-N-doped rGO with gradient microchannels 3D aerogel	rGO and Au NPs	Gradient microchannels and N for improving the ability	1	2.72	97.10%



				of water transport and evaporatio n			
115	2020	G/rGO nanosheets/PV A hydrogel	G/rGO nanosheets		1	1.44	86.00%
26	2020	Plasmonic Cu <sub>7</sub> S <sub>4</sub> -MoS <sub>2</sub> -Au NPs/PDMS	Plasmonic Cu <sub>7</sub> S <sub>4</sub> -MoS <sub>2</sub> -Au NPs		1	3.824	96.60%
52	2020	MOS <sub>2</sub> /PU/hydr ophilic PDA	MOS <sub>2</sub>		1	1.087	86.20%
174	2020	Hollow C nanospheres/p orous mixed cellulose ester membrane	Hollow C nanospheres		1	2	92.70%
116	2020	Rgo/KGM 3D porous sponge	rGO		1	1.6	92.00%
77	2020	CuS/bacterial cellulose (BC) hybrid gel membranes	CuS and BC- wrapped PE foam as heat insulation layer	BC- wrapped PE foam as water transport layer	1	1.79	98.50%
50	2020	Mesoporous CuO	Mesoporous CuO		1		83.66%
125	2020	CNTs/PAM hydrogel	CNTs		1	1.42	96.00%
175	2020	Self-floating H <sub>1.68</sub> MoO <sub>3</sub> /airl aid paper photothermal film	H <sub>1.68</sub> MoO <sub>3</sub>		1	1.37	87.80%
105	2021	A spring wrapped with Rgo/SA@cotto n towel	rGO		1	7.6	178.60%
97	2021	ACET doped PAM/SA- LN(25) dual- crosslinked hydrogel	ACET	Vertically aligned channels via direction freezing treatment	1	1.64483	93.00%
46	2021	MnO <sub>2</sub> nanowires/chit osan hydrogel	MnO <sub>2</sub> nanowires	Vertically aligned macropore assembly and low- tortuosity porous structure	1	1.78	90.60%

121	2021	2-layered hydrogel with MWCNTs-COOH/PVA hydrogel as bottom layer and hydrophobic PDMS as top layer	MWCNTs	Janus	1	1.34	85.71%
106	2021	Graphene/PS/PVA	Graphene		1	1.77	92.00%
107	2021	rGO/CA hydrogel	rGO		1	1.47	77.00%
136	2021	Ppy/polyvalent cations crosslinked alginate hydrogel with styrofoam for floating	PPy		1	1.15	54.12%
137	2021	BTA-doped PPy hydrogel	PPy and PS foam as a thermal insulator	Hydrophilic BTA and hydrophilic paper used to draw water	1	1.98	89.00%
138	2021	PPy/PAAM/chitosan gradient structured hydrogel	PPy particles	Introduced bubbles and micron-sized pores	1	2.41	92.00%
157	2021	Ni@C@SiO <sub>2</sub> core-shell NPs/PVA hydrogel composite film	Ni@C@SiO <sub>2</sub> core-shell NPs and rough surface by applying external magnetic field		1	2.25	91.20%
95	2021	bacterial cellulose-based cellulose nanofibrils hydrogels+aerogels	glutaraldehyde (GA)+CB NPs		1	1.82(4,32 light condition m/s)	in air 4 95.00%
56	2021	Bi <sub>2</sub> S <sub>3</sub> /Pd PAAH (polyacrylamide/polyacrylic acid hydrogel)	Bi <sub>2</sub> S <sub>3</sub> /Pd composite		1	1.61	97.00%
117	2021	GO/PEI/PEG	GO		1	1.32	88.00%
94	2021	CB/PVA hydrogel	CB		1	2.4	75.00%
173	2021	BiVO <sub>4</sub> -rGO hydrogel	BiVO <sub>4</sub> -rGO		1	1.6	87.00%

74	2021	Ag@carbonized melamin foam/MF	Ag@CMF	MF	1	2.39	119.46%
151	2021	Suedette sponge/filter paper/polydopamine	Polydopamine (PDA)	Filter paper (water restrictive layer) and suedette sponge (water storage layer)	1	1.8	92.00%
41	2021	Chitosan/gelatin-based IPN sponge incorporated with melanin-coated titania hollow nanospheres	Melanin-TiO <sub>2</sub> nanospheres		1	1.13	78.90%
142	2021	PPy coating on the spike of <i>Setaria viridis</i>	PPy	Spike of <i>Setaria viridis</i>	1	3.72	
78	2021	CuS/BC and BC biofoam	CuS		1	1.44	83.50%
162	2021	GO-rGO janus membrane	GO-rGO		1	1.836	91.40%
130	2021	CDs@Cotton fibers	CDs		1	2.32	93.60%
160	2021	PS-cellulose-PDA-PPy-PDA sphere	PPy; almost all the water only transport in the outer layers to reduce heat loss		1	2.6	
156	2021	COF/PDMS sponge	Benzoxazole-linked COF		1	1.39	84.70%
126	2021	Cellulose-reinforced tannin-functionalized aerogel coated with CNTs	CNTs		1	1.2	74.46%
118	2021	Nanofibrous CA/PMAA hydrogel-rGO membrane	rGO	Experimentally proven the presence of IW for lowering evaporation enthalpy	1	1.85	95.40%
132	2021	Assembling CDs on vertically aligned acetate fibers	CDs on the surface layer		1	2.6	93.90%

80	2021	Cu/carbon cell/PVA hydrogel	Cu/pollen cell derived carbon cells on the surface layer		1	2.08	93.43%
178	2021	Polyurethane (PU) sponge with black hydrogel skin	Chelation between TA and Fe <sup>3+</sup> in black hydrogel composed of tannic acid (TA), polyvinylpyrrolidone (PVP) and Fe <sup>3+</sup>	High porosity of the sponge and TA lower the evaporation enthalpy	1	2.8	94.00%
63	2021	Ti <sub>3</sub> C <sub>2</sub> T <sub>x</sub> (MXene) /La <sub>0.5</sub> Sr <sub>0.5</sub> CoO <sub>3</sub> (LSC) nanohetero-structures integrated with PVA/CTS hydrogel	Ti <sub>3</sub> C <sub>2</sub> T <sub>x</sub> (MXene)		1	2.73	92.30%
143	2021	Poly(sodium acrylate) (PSA) /PPy cryogels	PPy		1	1.41	96.90%
153	2021	PVA-PDA network	PDA	Millineedle array on the surface for steam release	1	2.94	94.50%
144	2021	PVA/PPy hydrogel membrane with micro-tree array	PPy	Micro-tree array for water collection in air	1	3.64	96.00%
67	2021	STA-EGaIn/lignin-CNC aerogel (SLC aerogel) with the inverted pyramid topography	Narrow the bandgap of Ga <sub>2</sub> O <sub>3</sub> (on the surface of EGaIn) using stearic acid; Pyramid topography surface		1	1.38	~94%
53	2021	Boron nanosheets modified with MoS <sub>2</sub> ) in a konjac glucomannan (KGM) sponge	Boron nanosheets modified with MoS <sub>2</sub> )		1	1.538	96.50%
54	2021	Composite hydrogel MoS <sub>2</sub> @Graphene	MoS <sub>2</sub> nanoflowers and Graphene	Controllable self-pumping system	0.9	3.2	
145	2021	Nanofibrous PVA based	PPy NPs and GO		1	2.87	87.50%

		membrane (NPM) with PPy NPs and GO					
47	2021	Chitin membrane with MnO <sub>2</sub> or CuO	MnO <sub>2</sub> or CuO	1	1.526 or 1.531	95.77% or 96.08%	
150	2021	Polyetherimide (PEI) modified cation exchange resin (CER) and PEDOT based conductive ink (EL-P 3040)	PEDOT based conductive ink (EL-P 3040)	1	1.42	~82%	
119	2021	Layered Graphene/poly methylmethacrylate composited membrane by electrospinning	Layered Graphene	1	1.25	~84%	
86	2021	Carbonized aerogels	Carbonized aerogels	1	2.1		
87	2021	Flexible carbon cloth nanocomposite with a biomimetic pelargonium hortorum-petal-like surface	Biomimetic flower-like carbon cloth (CC) nanocomposite	1	1.484	93.00%	
43	2021	Black titania/bacterial nanocellulose	Broad-spectrum active black titania (BT) NPs	1	1.71 ± 0.07	84.30 ± 3.40%	
64	2021	PDA/Ti <sub>3</sub> C <sub>2</sub> Tx MXene in a cellulose network skeleton of delignified wood (DW)	PDA and Ti <sub>3</sub> C <sub>2</sub> Tx MXene	1	2.08	93.60%	
93	2021	Carbonized corn straw	Carbonized corn straw	Vascular bundles and screens in corn straw	1	1.422	89.30%
66	2021	Copper-zinc-tin-selenide (CZTSe) nanocarambol as deposited on a hydrophilic	CZTSe	1	1.528	86.40%	



		filter membrane						
176	2021	Ni/C/Si core-shell sphere (SSA-Ni) film	Ni/C/Si core-shell sphere (SSA-Ni)		1	1.52	~91%	
127	2021	Multi-functional carbon nanotube paper	CNTs		1	1.28	~82%	
177	2021	Versatile carbon hybrid aerogel	C		1	2.1	89.80%	
154	2021	Mussel-inspired PDA-filled cellulose aerogel	PDA		1	1.36	86%	
170	2021	A cellulose paper directly with a pencil tracing and coating on surface	Pencil graphite		1	1.28	86.48%	
79	2021	Polyacrylamide (PAAm)/carboxymethyl cellulose (CMC)/CuS membrane	CuS		1	1.613	79%	
158	2021	Ti <sub>3</sub> C <sub>2</sub> T <sub>x</sub> MXene/rGO-embedded PVA hydrogel	Ti <sub>3</sub> C <sub>2</sub> T <sub>x</sub> MXene/rGO; Concave pyramidshaped surface topography		1	3.62	91%	
168	2021	Red mud/PVA/CTS gel	Red mud		1	2.185	90.74%	
120	2021	rGO based COF hydrogel	rGO and COF		1	1.47	92.07%	
88	2021	Janus monolithic chitosan scaffold (CS) aerogel with carbonized surface	Carbonized CTS surface	Continuous aligned run-through microchannels in Janus aerogel	1	1.76	91%	
99	2021	A 3D asymmetric evaporator by coating two CB/ PVA functional films with different channel structures and	CB		1	1.93		

		water uptake at two opposite sides					
179	2021	Nanocarbon/PVA	Nanocarbon	Submillimeter apertures	1	1.67	86.8%
180	2021	Co-Sn alloy@PTFE film	Co-Sn alloy		1	0.76	89%
181	2021	Catechol-functionalized chitosan with quinone-anchored AC	Quinone-anchored AC		1	3.4	~91%
159	2021	PPy/PVA-F Janus aerogel with rough hydrophobic upper layer and smooth hydrophilic bottom layer	PPy	Janus	1	1.68	94.7%
146	2021	PP-PDA/KH <sub>550</sub> /TiO <sub>2</sub> membrane with PPy on the outer surface	PPy on the outer surface	Capillary-driven siphon	1	3.65	229.13%
128	2021	CNTs/PPy/PS foam with fluorinated hydrophobic coating on the surface	CNTs and PPy		1	1.61	91.20%
169	2021	Semi-coke/PDA@melamine sponge	Semi-coke		1	1.41	90.56%
166	2021	Zwitterionic hydrogel coated PU//CNTs/PS foam/ cotton swabs	CNTs	The zwitterionic coating can form a hydration layer, leading to stable water transport.	1	2.2	93.50%
155	2021	DPP-2T/PVA	DPP-2T		1	2.6	89.00%

## Conclusions

In conclusion, recent progress in solar water purification proves that a higher evaporation rate and energy conversion

efficiency can be achieved by designing the entire system from two key aspects of heat and water management. As for the heat management, tailoring surface topography to enhance light harvesting, selecting adequate solar absorbers with stronger full solar spectrum absorption (especially the infrared band) and higher photothermal conversion ability, and minimizing heat

loss to the atmosphere and bulk water through managing the distribution of solar absorbers and heat insulation components, proved to be effective strategies for harvesting sunlight. Concerning water management, adjusting wettability to ensure rapid water replenishment, tuning the size, direction and structure of the internal channel to enhance the channel pumping, and increasing the IW content in hydrogels to lower the water vaporization enthalpy are the three main approaches that have been successfully implemented. However, it is still a challenge to maximize the evaporation rate and energy conversion efficiency concurrently, requiring coordination from chemistry, materials, engineering and other aspects. Additionally, lower capital and operating costs, better anti-fouling performance, self-floating capability, biomimetic design and additional integrated functions are the possible future development directions.

## Conflicts of interest

There are no conflicts to declare.

## Acknowledgements

Qiang Fu acknowledges the Australian Research Council under the Future Fellowship (FT180100312). Shudi Mao acknowledges support from the China Scholarship Council (CSC) Scholarship (202006140015).

## Notes and references

1. D. N. Chakkaravarthy, *International Journal of Agriculture Environment and Biotechnology*, 2019, **12**, 187-193.
2. W. W. Immerzeel, L. P. Van Beek and M. F. Bierkens, *Science*, 2010, **328**, 1382-1385.
3. Y. Wada, M. Flörke, N. Hanasaki, S. Eisner, G. Fischer, S. Tramberend, Y. Satoh, M. Van Vliet, P. Yillia and C. Ringler, *Geoscientific Model Development*, 2016, **9**, 175-222.
4. C. A. Schlosser, K. Strzepek, X. Gao, C. Fant, É. Blanc, S. Paltsev, H. Jacoby, J. Reilly and A. Gueneau, *Earth's Future*, 2014, **2**, 341-361.
5. P. Goh, A. Ismail and N. Hilal, in *Oxford Research Encyclopedia of Environmental Science*, 2019.
6. A. Panagopoulos, K.-J. Haralambous and M. Loizidou, *Science of The Total Environment*, 2019, **693**, 133545.
7. R. Semiat, *Environmental science & technology*, 2008, **42**, 8193-8201.
8. A. D. Khawaji, I. K. Kutubkhanah and J.-M. Wie, *Desalination*, 2008, **221**, 47-69.
9. F. A. AlMarzooqi, A. A. Al Ghaferi, I. Saadat and N. Hilal, *Desalination*, 2014, **342**, 3-15.
10. R. M. Morris, *Desalination*, 1993, **93**, 57-68.
11. H. Bamufleh, F. Abdelhady, H. M. Baaqeel and M. M. El-Halwagi, *Desalination*, 2017, **408**, 110-118.
12. A. Al-Karaghoul and L. L. Kazmerski, *Renewable Sustainable Energy Reviews*, 2013, **24**, 343-356.
13. M. Qasim, M. Badrelzaman, N. N. Darwish, N. A. Darwish and N. Hilal, *Desalination*, 2019, **459**, 59-104.
14. H. Strathmann, *Desalination*, 2010, **264**, 268-288.
15. J. R. Werber, A. Deshmukh and M. Elimelech, *Environmental Science & Technology Letters*, 2016, **3**, 112-120.
16. R. Zhao, S. Porada, P. Biesheuvel and A. Van der Wal, *Desalination*, 2013, **330**, 35-41.
17. N. Ghaffour, T. M. Missimer and G. L. Amy, *Desalination*, 2013, **309**, 197-207.
18. C. Y. Tang, Z. Yang, H. Guo, J. J. Wen, L. D. Nghiem and E. Cornelissen, *Environ Sci Technol*, 2018, **52**, 10215-10223.
19. N. A. A. Qasem, S. M. Zubair, B. A. Qureshi and M. M. Generous, *Energy Conversion and Management*, 2020, **205**.
20. S. Al-Amshawee, M. Y. B. M. Yunus, A. A. M. Azoddein, D. G. Hassell, I. H. Dakhil and H. A. Hasan, *Chemical Engineering Journal*, 2020, **380**.
21. H. C. Duong, L. Xia, Z. Ma, P. Cooper, W. Ela and L. D. Nghiem, *Journal of Membrane Science*, 2017, **542**, 133-142.
22. S. Sharshir, G. Peng, L. Wu, F. Essa, A. Kabeel and N. Yang, *Applied energy*, 2017, **191**, 358-366.
23. Y. Zhang, M. Sivakumar, S. Yang, K. Enever and M. Ramezani-pour, *Desalination*, 2018, **428**, 116-145.
24. Y. Guo, X. Zhou, F. Zhao, J. Bae, B. Rosenberger and G. Yu, *ACS Nano*, 2019, **13**, 7913-7919.
25. F. Zhao, X. Zhou, Y. Shi, X. Qian, M. Alexander, X. Zhao, S. Mendez, R. Yang, L. Qu and G. Yu, *Nat Nanotechnol*, 2018, **13**, 489-495.
26. H. Wang, R. Zhang, D. Yuan, S. Xu and L. Wang, *Advanced Functional Materials*, 2020, **30**, 2003995.
27. X. Zhang, Y. Peng, L. Shi and R. Ran, *ACS Sustainable Chemistry & Engineering*, 2020, **8**, 18114-18125.
28. D. Lapotko, *Optics express*, 2009, **17**, 2538-2556.
29. Z. Xu, Z. Li, Y. Jiang, G. Xu, M. Zhu, W.-C. Law, K.-T. Yong, Y. Wang, C. Yang, B. Dong and F. Xing, *Journal of Materials Chemistry A*, 2020, **8**, 25571.
30. M. Gao, L. Zhu, C. K. Peh and G. W. Ho, *Energy & Environmental Science*, 2019, **12**, 841-864.
31. L. Zhu, M. Gao, C. K. N. Peh and G. W. Ho, *Nano Energy*, 2019, **57**, 507-518.
32. M. Tan, J. Wang, W. Song, J. Fang and X. Zhang, *Journal of Materials Chemistry A*, 2019, **7**, 1244-1251.
33. Y. Guo, H. Lu, F. Zhao, X. Zhou, W. Shi and G. Yu, *Adv Mater*, 2020, **32**, 1907061.
34. Y. Guo, X. Zhao, F. Zhao, Z. Jiao, X. Zhou and G. Yu, *Energy & Environmental Science*, 2020, **13**, 2087-2095.
35. F. Yu, Y. Chen, X. Liang, J. Xu, C. Lee, Q. Liang, P. Tao and T. Deng, *Progress in natural science: Materials International*, 2017, **27**, 531-542.
36. Y. Zhao and C. Burda, *Energy Environmental Science*, 2012, **5**, 5564-5576.
37. F. Zhao, Y. Guo, X. Zhou, W. Shi and G. Yu, *Nature Reviews Materials*, 2020, **5**, 388-401.
38. C. M. Hessel, V. P. Pattani, M. Rasch, M. G. Panthani, B. Koo, J. W. Tunnell and B. A. Korgel, *Nano letters*, 2011, **11**, 2560-2566.
39. A. Standard, *Ann. Book of ASTM Standards*, 2012, **14**, 1-20.
40. Z. Sun, Z. Li, W. Li and F. Bian, *Cellulose*, 2019, **27**, 481-491.
41. X. Wang, Z. Li, Y. Wu, H. Guo, X. Zhang, Y. Yang, H. Mu and J. Duan, *ACS Appl Mater Interfaces*, 2021, **13**, 10902-10915.
42. X. Zhang, X. Wang, W. D. Wu, X. D. Chen and Z. Wu, *Journal of Materials Chemistry A*, 2019, **7**, 6963-6971.

43. K. Nabeela, M. N. Thorat, S. N. Backer, A. M. Ramachandran, R. T. Thomas, G. Preethikumar, A. P. Mohamed, A. Asok, S. G. Dastager and S. Pillai, *ACS Applied Bio Materials*, 2021, **4**, 4373-4383.
44. C. Dette, M. A. Pérez-Osorio, C. S. Kley, P. Punke, C. E. Patrick, P. Jacobson, F. Giustino, S. J. Jung and K. Kern, *Nano letters*, 2014, **14**, 6533-6538.
45. J. Tao, T. Luttrell and M. Batzill, *Nature chemistry*, 2011, **3**, 296-300.
46. M. S. Irshad, X. Wang, M. S. Abbasi, N. Arshad, Z. Chen, Z. Guo, L. Yu, J. Qian, J. You and T. Mei, *ACS Sustainable Chemistry & Engineering*, 2021, **9**, 3887-3900.
47. X. Li, J. Huang, L. Guo, X. Jin, L. Wang, Y. Deng, H. Xie and L. Ye, *Inorganic Chemistry Communications*, 2021, **129**, 108651.
48. P. Wang, Y. Gu, L. Miao, J. Zhou, H. Su, A. Wei, X. Mu, Y. Tian, J. Shi and H. Cai, *Sustainable Materials and Technologies*, 2019, **20**, e00106.
49. F. L. Meng, M. Gao, T. Ding, G. Yilmaz, W. L. Ong and G. W. Ho, *Advanced Functional Materials*, 2020, **30**, 2002867.
50. H. Zhang, K. Wang, L. Wang, H. Xie and W. Yu, *Solar Energy*, 2020, **201**, 628-637.
51. C. Li, L. Fan, R. Zhu, X. Li, P. Wen, X. Zhao, G. Wang, J. Zou and F. Kim, *ACS Applied Energy Materials*, 2020, **3**, 9216-9225.
52. Q. Wang, F. Jia, A. Huang, Y. Qin, S. Song, Y. Li and M. A. C. Arroyo, *Desalination*, 2020, **481**, 114359.
53. J. Yin, X. You, Z. Zhang, Z. Guo, J. Wang and X. Wang, *Journal of Water Process Engineering*, 2021, **41**, 102048.
54. Y. Li, X.-I. Shi, L.-j. Sun, M. Zhao, T. Jiang, W. Jiang, M. Deng, S. Yang and Y. Wang, *Desalination*, 2021, **515**, 115192.
55. Z. Guo, F. Yu, Z. Chen, Z. Shi, J. Wang and X. Wang, *Solar Energy Materials and Solar Cells*, 2020, **211**, 110531.
56. X. Geng, D. Zhang, Z. Zheng, G. Ye, S. Li, H. Tu, Y. Wan and P. Yang, *Nano Energy*, 2021, **82**, 105700.
57. H. Su, J. Zhou, L. Miao, J. Shi, Y. Gu, P. Wang, Y. Tian, X. Mu, A. Wei, L. Huang, S. Chen and Z. Deng, *Sustainable Materials and Technologies*, 2019, **20**, e00095.
58. L. Zhu, L. Sun, H. Zhang, D. Yu, H. Aslan, J. Zhao, Z. Li, M. Yu, F. Besenbacher and Y. Sun, *Nano Energy*, 2019, **57**, 842-850.
59. F. Yu, X. Ming, Y. Xu, Z. Chen, D. Meng, H. Cheng, Z. Shi, P. Shen and X. Wang, *Advanced Materials Interfaces*, 2019, **6**, 1901168.
60. S. Cao, J. Jiang, Q. Tian, C. Guo, X. Wang, K. Dai and Q. Xu, *Green Energy & Environment*, 2020, DOI: 10.1016/j.gee.2020.12.012.
61. W. Li, X. Li, W. Chang, J. Wu, P. Liu, J. Wang, X. Yao and Z.-Z. Yu, *Nano Research*, 2020, **13**, 3048-3056.
62. Z. Yu and P. Wu, *Advanced Materials Technologies*, 2020, **5**, 2000065.
63. D. Fan, Y. Lu, H. Zhang, H. Xu, C. Lu, Y. Tang and X. Yang, *Applied Catalysis B: Environmental*, 2021, **295**, 120285.
64. Y. Chen, J. Yang, L. Zhu, X. Jia, S. Wang, Y. Li and H. Song, *Journal of Materials Chemistry A*, 2021, **9**, 15482-15492.
65. Y. Yang, W. Que, J. Zhao, Y. Han, M. Ju and X. Yin, *Chemical Engineering Journal*, 2019, **373**, 955-962.
66. L. Yang, N. Li, C. Guo, J. He, S. Wang, L. Qiao, F. Li, L. Yu, M. Wang and X. Xu, *Chemical Engineering Journal*, 2021, **417**, 128051.
67. Z. Wei, C. Cai, Y. Huang, Y. Wang and Y. Fu, *Nano Energy*, 2021, **86**, 106138.
68. Z. W. Seh, S. Liu, M. Low, S. Y. Zhang, Z. Liu, A. Mlayah and M. Y. Han, *Advanced Materials*, 2012, **24**, 2310-2314.
69. M. Gao, P. K. N. Connor and G. W. Ho, *Energy Environmental Science*, 2016, **9**, 3151-3160.
70. L. Zhu, M. Gao, C. K. N. Peh and G. W. Ho, *Materials Horizons*, 2018, **5**, 323-343.
71. Z. Sun, J. Wang, Q. Wu, Z. Wang, Z. Wang, J. Sun and C. J. Liu, *Advanced Functional Materials*, 2019, **29**, 1901312.
72. C. Liu, C. Cai, F. Ma, X. Zhao and H. Ahmad, *J Colloid Interface Sci*, 2020, **560**, 103-110.
73. C. Xiao, W. Liang, Q.-M. Hasi, L. Chen, J. He, F. Liu, C. Wang, H. Sun, Z. Zhu and A. Li, *Materials Today Energy*, 2020, **16**, 100417.
74. Y. Shi, C. Zhang, Y. Wang, Y. Cui, Q. Wang, G. Liu, S. Gao and Y. Yuan, *Desalination*, 2021, **507**, 115038.
75. X. Meng, J. Yang, S. Ramakrishna, Y. Sun and Y. Dai, *Journal of Materials Chemistry A*, 2020, **8**, 16570-16581.
76. Y. Sun, J. Gao, Y. Liu, H. Kang, M. Xie, F. Wu and H. Qiu, *Chemical Engineering Science*, 2019, **207**, 516-526.
77. D. Zhang, Y. Cai, Q. Liang, Z. Wu, N. Sheng, M. Zhang, B. Wang and S. Chen, *ACS Sustainable Chemistry & Engineering*, 2020, **8**, 9017-9026.
78. D. Zhang, M. H. Zhang, S. Y. Chen, Q. Q. Liang, N. Sheng, Z. L. Han, Y. X. Cai and H. P. Wang, *Desalination*, 2021, **500**, 10.
79. J. Chen, D. Wang, X. Li, H. Sun, H. Zhao, Y. Li, X. Liu and G. Shi, *ACS Applied Polymer Materials*, 2021, **3**, 2402-2410.
80. C. Tian, C. Li, D. Chen, Y. Li, L. Xing, X. Tian, Y. Cao, W. Huang, Z. Liu and Y. Shen, *Journal of Materials Chemistry A*, 2021, **9**, 15462-15471.
81. Y. Guo, F. Zhao, X. Zhou, Z. Chen and G. Yu, *Nano letters*, 2019, **19**, 2530-2536.
82. X. Zhou, Y. Guo, F. Zhao, W. Shi and G. Yu, *Adv Mater*, 2020, **32**, 2007012.
83. J. Zeng, Q. Wang, Y. Shi, P. Liu and R. Chen, *Advanced Energy Materials*, 2019, **9**, 1900552.
84. X. Liang, X. Zhang, Q. Huang, H. Zhang, C. Liu and Y. Liu, *Solar Energy*, 2020, **208**, 778-786.
85. F. Gong, H. Li, W. Wang, J. Huang, D. Xia, J. Liao, M. Wu and D. V. Papavassiliou, *Nano Energy*, 2019, **58**, 322-330.
86. J. Liu, X. Chen, H. Yang, J. Tang, R. Miao, K. Liu and Y. Fang, *Materials Chemistry Frontiers*, 2021, **5**, 1953-1961.
87. Y. Xu, Z. Guo, J. Wang, Z. Chen, J. Yin, Z. Zhang, J. Huang, J. Qian and X. Wang, *ACS Applied Materials and Interfaces*, 2021, **13**, 27129-27139.
88. Z. Liu, R.-K. Qing, A.-Q. Xie, H. Liu, L. Zhu and S. Chen, *ACS Applied Materials and Interfaces*, 2021, **13**, 18829-18837.
89. X. Chen, Z. Wu, D. Lai, M. Zheng, L. Xu, J. Huo, Z. Chen, B. Yuan and M.-L. Fu, *Journal of Materials Chemistry A*, 2020, **8**, 22645-22656.
90. P.-F. Liu, L. Miao, Z. Deng, J. Zhou, H. Su, L. Sun, S. Tanemura, W. Cao, F. Jiang and L.-D. Zhao, *Materials Today Energy*, 2018, **8**, 166-173.
91. Y. Lu, X. Wang, D. Fan, H. Yang, H. Xu, H. Min and X. Yang, *Sustainable Materials and Technologies*, 2020, **25**, e00180.
92. Y. Long, S. Huang, H. Yi, J. Chen, J. Wu, Q. Liao, H. Liang, H. Cui, S. Ruan and Y.-J. Zeng, *Journal of Materials Chemistry A*, 2019, **7**, 26911-26916.
93. J. Feng, B. Bai, L. Yang, N. Hu and H. Wang, *Materials Chemistry and Physics*, 2021, **271**, 124904.
94. H. Lu, W. Shi, F. Zhao, W. Zhang, P. Zhang, C. Zhao and G. Yu, *Advanced Functional Materials*, 2021, **31**, 2101036.

95. N. Li, L. Qiao, J. He, S. Wang, L. Yu, P. Murto, X. Li and X. Xu, *Advanced Functional Materials*, 2021, **31**, 2008681.
96. Z. Deng, L. Miao, P.-F. Liu, J. Zhou, P. Wang, Y. Gu, X. Wang, H. Cai, L. Sun and S. Tanemura, *Nano Energy*, 2019, **55**, 368-376.
97. J. X. He, Y. K. Fan, C. H. Xiao, F. Liu, H. X. Sun, Z. Q. Zhu, W. D. Liang and A. Li, *Compos. Sci. Technol.*, 2021, **204**, 9.
98. N. Hu, Y. Xu, Z. Liu, M. Liu, X. Shao and J. Wang, *Carbohydr Polym*, 2020, **243**, 116480.
99. J. Liu, J. Gui, W. Zhou, X. Tian, Z. Liu, J. Wang, L. Yang, P. Zhang, W. Huang and J. Tu, *Nano Energy*, 2021, **86**, 106112.
100. X. Zhou, F. Zhao, Y. Guo, Y. Zhang and G. Yu, *Energy & Environmental Science*, 2018, **11**, 1985-1992.
101. P. Zhang, Q. Liao, H. Yao, H. Cheng, Y. Huang, C. Yang, L. Jiang and L. Qu, *Journal of Materials Chemistry A*, 2018, **6**, 15303-15309.
102. L. Zhao, P. Wang, J. Tian, J. Wang, L. Li, L. Xu, Y. Wang, X. Fei and Y. Li, *Sci Total Environ*, 2019, **668**, 153-160.
103. Y. Liu, J. Tian, L. Xu, Y. Wang, X. Fei and Y. Li, *New Journal of Chemistry*, 2020, **44**, 20181-20191.
104. P. Zhuang, D. Li, N. Xu, X. Yu and L. Zhou, *Global Challenges*, 2020, **5**, 2000053.
105. T. Gao, X. Wu, Y. Wang, G. Owens and H. Xu, *Solar RRL*, 2021, **5**, 2100053.
106. W. Lei, S. Khan, L. Chen, N. Suzuki, C. Terashima, K. Liu, A. Fujishima and M. Liu, *Nano Research*, 2021, **14**, 1135-1140.
107. G. Lou, Y. Wang, Y. Ma, J. Kou, F. Wu and J. Fan, *Frontiers of Materials Science*, 2021, **15**, 138-146.
108. C.-S. Hu, H.-J. Li, J.-Y. Wang, A. Haleem, X.-C. Li, M. Siddiq and W.-D. He, *ACS Applied Energy Materials*, 2019, **2**, 7554-7563.
109. B. Huo, D. Jiang, X. Cao, H. Liang, Z. Liu, C. Li and J. Liu, *Carbon*, 2019, **142**, 13-19.
110. X.-Y. Wang, J. Xue, C. Ma, T. He, H. Qian, B. Wang, J. Liu and Y. Lu, *Journal of Materials Chemistry A*, 2019, **7**, 16696-16703.
111. H. Geng, C. Lv, M. Wu, H. Ma, H. Cheng, C. Li, J. Yuan and L. Qu, *Glob Chall*, 2020, **4**, 2000043.
112. S. Hou, Y. Lv, X. Wu, J. Guo, Q. Sun, L. Wang and D. Jia, *New Journal of Chemistry*, 2020, **44**, 2228-2235.
113. Y. Kong, H. Dan, W. Kong, Y. Gao, Y. Shang, K. Ji, Q. Yue and B. Gao, *Journal of Materials Chemistry A*, 2020, **8**, 24734-24742.
114. X. Meng, J. Yang, S. Ramakrishna, Y. Sun and Y. Dai, *ACS Sustainable Chemistry & Engineering*, 2020, **8**, 4955-4965.
115. J. Tian, X. Huang and W. Wu, *Industrial & Engineering Chemistry Research*, 2020, **59**, 1135-1141.
116. K. Yu, P. Shao, P. Meng, T. Chen, J. Lei, X. Yu, R. He, F. Yang, W. Zhu and T. Duan, *J Hazard Mater*, 2020, **392**, 122350.
117. C. Liu, Y. Peng and X. Zhao, *Desalination*, 2021, **501**, 114911.
118. L. Zang, L. Sun, S. Zhang, C. Finnerty, A. Kim, J. Ma and B. Mi, *Chemical Engineering Journal*, 2021, **422**, 129998.
119. D. Li, X. Zhang, S. Zhang, D. Wang, Z. Wang, Y. Liu, X. Yu, Q. Zhao and B. Xing, *Chemosphere*, 2021, **267**, 128916.
120. C.-R. Zhang, W.-R. Cui, C.-P. Niu, S.-M. Yi, R.-P. Liang, J.-X. Qi, X.-J. Chen, W. Jiang, L. Zhang and J.-D. Qiu, *Chemical Engineering Journal*, 2021, **428**, 131178.
121. H. Jian, Q. Qi, W. Wang and D. Yu, *Separation and Purification Technology*, 2021, **264**, 118459.
122. W. Xu, Y. Xing, J. Liu, H. Wu, Y. Cui, D. Li, D. Guo, C. Li, A. Liu and H. Bai, *ACS Nano*, 2019, **13**, 7930-7938.
123. L. Zhu, T. Ding, M. Gao, C. K. N. Peh and G. W. Ho, *Advanced Energy Materials*, 2019, **9**, 1900250.
124. Q. F. Guan, Z. M. Han, Z. C. Ling, H. B. Yang and S. H. Yu, *Nano letters*, 2020, **20**, 5699-5704.
125. Y. Zhou, T. Ding, M. Gao, K. H. Chan, Y. Cheng, J. He and G. W. Ho, *Nano Energy*, 2020, **77**, 105102.
126. X. Luo, J. Zhang, J. Tao, X. Wang, S. Zhao, Z. Chen, S. Liu, J. Li and S. Li, *Chemical Engineering Journal*, 2021, **416**, 129486.
127. Y. Duan, M. Weng, W. Zhang, Y. Qian, Z. Luo and L. Chen, *Energy Conversion and Management*, 2021, **241**, 114306.
128. S. Sun, Y. Wang, B. Sun, F. Zhang, Q. Xu, H.-Y. Mi, H. Li, X. Tao, Z. Guo and C. Liu, *ACS Applied Materials and Interfaces*, 2021, **13**, 24945-24956.
129. Q. Zhao, T. Fan, J. Ding, D. Zhang, Q. Guo and M. Kamada, *Carbon*, 2011, **49**, 877-883.
130. W. Zhang, Q. Chang, C. Xue, J. Yang and S. Hu, *Solar RRL*, 2021, **5**, 2100133.
131. S. Singh, N. Shauloff and R. Jelinek, *ACS Sustainable Chemistry & Engineering*, 2019, **7**, 13186-13194.
132. H. Zhou, C. Xue, Q. Chang, J. Yang and S. Hu, *Chemical Engineering Journal*, 2021, **421**, 129822.
133. Indriyati, I. Primadona, F. A. A. Permatasari, M. A. Irham, D. E. M. nasir and F. Iskandar, *Nanoscale*, 2021, **13**, 7523-7532.
134. L. Xu, L. Cheng, C. Wang, R. Peng and Z. Liu, *Polymer Chemistry*, 2014, **5**, 1573-1580.
135. X. Zhou, F. Zhao, Y. Guo, B. Rosenberger and G. Yu, *Science Advances*, 2019, **5**, eaaw5484.
136. S. H. Park, J. H. Park, J. Kim and S. J. Lee, *Desalination*, 2021, **500**, 114900.
137. Y. Wu, L. Shen, C. Zhang, H. Gao, J. Chen, L. Jin, P. Lin, H. Zhang and Y. Xia, *Desalination*, 2021, **505**, 114766.
138. T. Xu, Y. Xu, J. Wang, H. Lu, W. Liu and J. Wang, *Chemical Engineering Journal*, 2021, **415**, 128893.
139. C. Li, D. Jiang, B. Huo, M. Ding, C. Huang, D. Jia, H. Li, C.-Y. Liu and J. Liu, *Nano Energy*, 2019, **60**, 841-849.
140. F. Ni, P. Xiao, C. Zhang, Y. Liang, J. Gu, L. Zhang and T. Chen, *ACS Appl Mater Interfaces*, 2019, **11**, 15498-15506.
141. W. Wang, J. Niu, J. Guo, L. Yin and H. Huang, *Solar Energy Materials and Solar Cells*, 2019, **201**, 110046.
142. Z. Xie, J. Zhu and L. Zhang, *ACS Appl Mater Interfaces*, 2021, **13**, 9027-9035.
143. S.-L. Loo, L. Vásquez, M. Zahid, F. Costantino, A. Athanassiou and D. Fragouli, *ACS Applied Materials and Interfaces*, 2021, **13**, 30542-30555.
144. Y. Shi, O. Ilic, H. A. Atwater and J. R. Greer, *Nature communications*, 2021, **12**, 1-10.
145. S. Chen, Y. Liu, Y. Wang, K. Xu, X. Zhang, W. Zhong, G. Luo and M. Xing, *Chemical Engineering Journal*, 2021, **411**, 128042.
146. C. Wei, X. Zhang, S. Ma, C. Zhang, Y. Li, D. Chen, H. Jiang, Z. Xu and X. Huang, *Chemical Engineering Journal*, 2021, **425**, 130118.
147. X. Yin, Y. Zhang, Q. Guo, X. Cai, J. Xiao, Z. Ding and J. Yang, *ACS Applied Materials & Interfaces*, 2018, **10**, 10998-11007.
148. F. Zhu, L. Wang, B. Demir, M. An, Z. L. Wu, J. Yin, R. Xiao, Q. Zheng and J. Qian, *Materials Horizons*, 2020, **7**, 3187-3195.
149. X. Zhao and C. Liu, *Desalination*, 2020, **482**, 114385.
150. C. Liu, Y. Peng, C. Cai, J. Zhang and X. Zhao, *Journal of Environmental Chemical Engineering*, 2021, **9**, 105272.



151. Y. Sun, X. Zong, D. Qu, G. Chen, L. An, X. Wang and Z. Sun, *Journal of Materials Chemistry A*, 2021, **9**, 7122-7128.
152. X. Xu, S. Ozden, N. Bizmark, C. B. Arnold, S. S. Datta and R. D. Priestley, *Adv Mater*, 2021, **33**, 2007833.
153. Z. Huang, J. Wei, Y. Wan, P. Li, J. Yu, J. Dong, S. Wang, S. Li and C. S. Lee, *Small*, 2021, DOI: 10.1002/sml.202101487, 2101487.
154. Y. Zou, J. Zhao, J. Zhu, X. Guo, P. Chen, G. Duan, X. Liu and Y. Li, *ACS Applied Material and Interfaces*, 2021, **13**, 7617-7624.
155. Q. Zhao, Z. Huang, Y. Wan, J. Tan, C. Cao, S. Li and C.-S. Lee, *Journal of Materials Chemistry A*, 2021, **9**, 2104-2110.
156. W. R. Cui, C. R. Zhang, R. P. Liang, J. Liu and J. D. Qiu, *ACS Appl Mater Interfaces*, 2021, **13**, 31561-31568.
157. F. Yang, J. X. Chen, Z. Y. Ye, D. W. Ding, N. V. Myung and Y. D. Yin, *Advanced Functional Materials*, 2021, **31**, 9.
158. Y. Lu, D. Fan, Y. Wang, H. Xu, C. Lu and X. Yang, *ACS nano*, 2021, **15**, 10366-10376.
159. B. Wen, X. Zhang, Y. Yan, Y. Huang, S. Lin, Y. Zhu, Z. Wang, B. Zhou, S. Yang and J. Liu, *Desalination*, 2021, **516**, 115228.
160. X. Wu, Y. Wang, P. Wu, J. Zhao, Y. Lu, X. Yang and H. Xu, *Advanced Functional Materials*, 2021, DOI: 10.1002/adfm.202102618.
161. L. Zhao, J. Tian, Y. Liu, L. Xu, Y. Wang, X. Fei and Y. Li, *Environmental Science: Water Research & Technology*, 2020, **6**, 221-230.
162. H. Zhang, H. Xie, W. Han, X. Yan, X. Liu, L. He, P. Lin, Y. Xia, K. Zhang, J. A. Zapien and K.-B. Yoon, *ACS Applied Nano Materials*, 2021, **4**, 1916-1923.
163. F. Yu, Z. Chen, Z. Guo, M. S. Irshad, L. Yu, J. Qian, T. Mei and X. Wang, *ACS Sustainable Chemistry & Engineering*, 2020, **8**, 7139-7149.
164. X. Liang, X. Zhang, Z. Liu, Q. Huang, H. Zhang, C. Liu and Y. Liu, *Solar Energy*, 2020, **201**, 581-588.
165. Y. Guo and G. Yu, *Accounts of Materials Research*, 2021, **2**, 374-384.
166. C. Wen, H. Guo, J. Yang, Q. Li, X. Zhang, X. Sui, M. Cao and L. Zhang, *Chemical Engineering Journal*, 2021, **421**, 130344.
167. Y. Xu, X. Xiao, X. Fan, Y. Yang, C. Song, Y. Fan and Y. Liu, *Journal of Materials Chemistry A*, 2020, **8**, 24108-24116.
168. P. Wang, X. Wang, S. Chen, J. Zhang, X. Mu, Y. Chen, Z. Sun, A. Wei, Y. Tian and J. Zhou, *ACS Applied Materials and Interfaces*, 2021, **13**, 30556-30564.
169. L. Zhang, X. Xu, J. Feng, B. Bai, N. Hu and H. Wang, *Solar Energy Materials and Solar Cells*, 2021, **230**, 111237.
170. M. Z. Tariq, Z. Hanif, M. La, D. Choi and S. J. Park, *International Journal of Energy Research*, 2021, **45**, 6395-6404.
171. J. J. Koh, G. J. H. Lim, S. Chakraborty, Y. Zhang, S. Liu, X. Zhang, S. C. Tan, Z. Lyu, J. Ding and C. He, *Nano Energy*, 2021, **79**, 105436.
172. P.-F. Liu, L. Miao, Z. Deng, J. Zhou, Y. Gu, S. Chen, H. Cai, L. Sun and S. Tanemura, *Applied Energy*, 2019, **241**, 652-659.
173. L. L. Noreen, Z. J. Xie, M. Hussain, M. M. Li, Q. Q. Lyu, K. Wang, L. B. Zhang and J. T. Zhu, *Solar Energy Materials and Solar Cells*, 2021, **222**, 7.
174. H. Yang, G. Yang, Z. Qiao, H. Bao, S. Zhang, X. Li and Y. Liu, *ACS Appl Mater Interfaces*, 2020, **12**, 35193-35200.
175. Q. Zhu, K. Ye, W. Zhu, W. Xu, C. Zou, L. Song, E. Sharman, L. Wang, S. Jin, G. Zhang, Y. Luo and J. Jiang, *J Phys Chem Lett*, 2020, **11**, 2502-2509.
176. D. Ding, H. Wu, X. He, F. Yang, C. Gao, Y. Yin and S. Ding, *Journal of Materials Chemistry A*, 2021, **9**, 11241-11247.
177. Z. Huang, Y. Wan, J. Liang, Y. Xiao, X. Li, X. Cui, S. Tian, Q. Zhao, S. Li and C.-S. Lee, *ACS Applied Materials and Interfaces*, 2021, **13**, 31624-31634.
178. Z. Wang, X. Wu, J. Dong, X. Yang, F. He, S. Peng and Y. Li, *Chemical Engineering Journal*, 2022, **427**, 130905.
179. Y. Li, W. Hong, H. Li, Z. Yan, S. Wang, X. Liu, B. Li, H. Jiang and X. Niu, *Desalination*, 2021, **511**, 115113.
180. Y. Wang, L. Zhao, F. Zhang, K. Yu, C. Yang, J. Jia, W. Guo, J. Zhao and F. Qu, *ACS Applied Materials and Interfaces*, 2021, **13**, 26879-26890.
181. Y. Guo, C. M. Dundas, X. Zhou, K. P. Johnston and G. Yu, *Advanced Materials*, 2021, DOI: 10.1002/adma.202102994, 2102994.

1